Three-dimensional modeling of solidification grain structures generated by laser powder bed fusion

Th. Camus, Daniel Maisonnette, Oriane Baulin, Oriane Senninger, Gildas Guillemot, Charles-André Gandin

Three-dimensional modeling of solidification grain structures generated by laser powder bed fusion

Th. Camus[(1,2)], D. Maisonnette[(2)], O. Baulin[(2)], O. Senninger[(1)], G. Guillemot[(1)], Ch.-A. Gandin[(1)*]

(1) Mines Paris, PSL University, CEMEF UMR CNRS 7635, 06904 Sophia Antipolis, France
(2) Cetim, 7 rue de la Presse, 42000 Saint-Etienne, France

Abstract

Grain structures generated by laser powder bed fusion (L-PBF) of the Ni-based superalloy Inconel 718 (IN718) are studied using Cellular Automaton modelling. A new hybrid methodology is developed to benefit from a full thermohydraulic simulations that predicts the shape of the consolidated track and the temperature field. The advantage is to reach unprecedented sizes of simulation domains while still taking advantage of a full numerical solution of the L-PBF process at the scale of the melt pool. The computed grain structure becomes available in a Representative Elementary Volume (REV) of an Additively Manufactured (AMed) specimen and can be studied statistically considering the distribution of crystallographic orientations and the grain density. The other advantage is the possibility to vary process and material parameters to approach industrial practice. For the first time, the strategy consisting in opposite bidirectional scanning of the powder with an additional 67° rotation at each new layer is made available. It is compared with the standard opposite bidirectional monoaxial scanning strategy and the opposite bidirectional orthogonal biaxial scanning strategies with two perpendicular axes, all reproducing trends reported in experimental literature. The generation of virtual REVs of AMed microstructures by L-PBF for IN718 opens the way to study new processing parameters and coupling with models for the prediction of metallurgical properties.

Graphical abstract

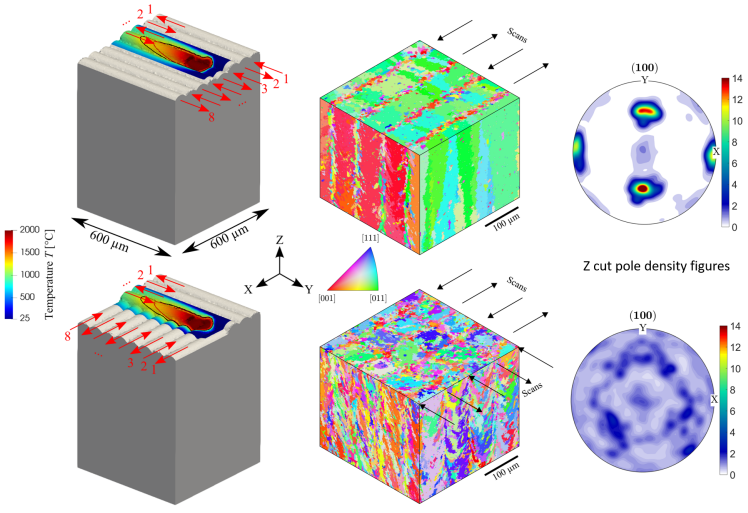

Keywords: Additive Manufacturing, Grain Structure, Texture, Modeling, Inconel 718

*Corresponding author
Email address: charles-andre.gandin@minesparis.psl.eu (Ch.-A. Gandin[(1)])

1. Introduction

Additive manufacturing (AM) processes produce parts by deposition of layers. They are notably developed as an answer to industrial needs for complex geometries [1, 2]. Among AM processes, the Laser Powder Bed Fusion (L-PBF) process has become dominant for metallic materials. A powder is spread on the top surface of the part under construction. A laser locally melts the powder and an underneath portion of the part. Its solidification creates a consolidated layer with tight connection with already built layers. The scanning strategy of the laser is defined for each layer, accounting for its boundaries computed from a section of the three-dimensional (3D) computer aided design model of the part. Once fully scanned, the surface is covered by another layer of powder and the process is repeated one after another until achievement of the desired Additively Manufactured (AMed) geometry. L-PBF was initially developed for fast prototyping. It is now being introduced as a production process to achieve designs that cannot be reached by conventional processes. AMed parts by L-PBF are primarily used for high added value applications, in medical, automotive and aerospace sectors [3].

Inconel 718 (IN718) is a Ni-based superalloy widely used to manufacture discs and gas turbine blades for aircraft engines due to its good mechanical properties at high temperatures [4]. Its machining is difficult and must be carried out at temperatures above 540 °C. Residual stresses are generated in the parts, and the machining tools wear out very quickly. The production of parts by casting also has drawbacks as uncontrolled porosities or segregations may appear during casting, which deteriorates the mechanical properties. The use of AMed IN718 parts produced by L-PBF has consequently focused great attention for more than a decade [4, 5, 6, 7, 8, 9, 10, 11, 12, 13, 14, 15, 16, 17, 18].

In L-PBF, a melt pool develops during laser scanning as the powder and underneath previously solidified layers are locally melted. Analogies of the heat flow with welding is very common and the use of dedicated analytical heat flow solutions [19, 20] is not rare in the literature [21, 22]. Assuming that the melt pool is delimited by the contour surface of the liquidus isotherm of the alloy, T_L, the temperature gradient drawn on this isotherm, G_L, is oriented toward the center of the melt pool. The local isotherm velocity computed on the T_L contour, v_L, is only directed inward the melt pool where cooling and solidification take place, i.e. in the aftermath of the laser also defining the rear of the pool. A similar analysis can be performed for the solidus isotherm, T_S [°C or K], both liquidus and solidus temperatures representing the solidification interval of the alloy where a mushy zone develop [23]. As a result, one can extract criteria for the size and the morphology of the microstructure [2] by exploiting classical physical metallurgy models [23, 24]. A simplified representation concludes that, under steady growth conditions, the size of a dendritic microstructure is inversely proportional to the cooling rate, $|G_L\, v_L|$. With respect to the grain morphology, the analogy with welding processing is still valid. Columnar grains can epitaxially grow from pre-existing grains that are partially melted at the boundaries of the melt pool. For a simple opposite bidirectional monoaxial scanning strategy of the laser, a columnar grain structure was characterized by a $\langle 100 \rangle$, fiber texture aligned with the scanning directions together with a $\langle 110 \rangle$, fiber texture in the building direction of the part [15, 16, 17]. These observations are directly related to the measured anisotropic mechanical properties. The crystallographic texture can be controlled through the strategy of laser scanning [14] and the process parameters. Equiaxed grains can also form in the pool and compete with the growth of the columnar grains. A transition between columnar and equiaxed grains is expected when the ratio $|G_L/v_L|$ decreases [25]. These trends, well known and modeled since the 80's, were applied to laser processing from the 90's so as to produce single crystals [26] and now AMed materials by L-PBF [27, 28, 29]. While such description can be very useful, it does not offer a direct 3D representation of the grain structure, including its crystallographic texture and morphology. Modelling can help to understand these links and accelerate the search for texture optimization.

As the heat flow is the prime parameter controlling the AMed microstructure, an advanced model for

L-PBF is required that can reflect the effect of the processing parameters is required. However, it needs to be coupled with a method dedicated to the simulation of solidification microstructures. Literature reviews on modeling of microstructure for additive manufacturing consider several classes of methodologies [30, 31]. The Phase Field (PF) method is very powerful to predict the growth of dendritic microstructures in metallic alloys [32]. Applications to 3D simulations for multicomponent alloys yet remain limited. This is due to the computational cost to reach the size of a Representative Elementary Volume (REV) containing enough information to describe the grain structure anisotropy while maintaining a sufficiently refined description of the solid-liquid interface. This assertion is true even when exploiting high performance computing facilities [33]. Despite these limitations, tentative is available, often restricted to two-dimensional (2D) analyses and focusing on dedicated phenomena such as interdendritic segregation [34, 35] or planar front solidification [36]. With the goal to reaching larger domain sizes while still solving the diffusion field in the liquid surrounding the dendrite tip that controls the growth kinetics, alternative methodologies have been developed. They include the grain envelope model [37, 38, 39, 40], the dendritic needle network method [41, 42, 43] and the hybrid cellular automaton – parabolic thick needle method [44]. However, they can still hardly be applied to generate a REV of AMed microstructures by L-PBF for IN718.

Models were also proposed to simplify the description of the grains by avoiding a direct representation of the underlying dendritic microstructure. The Monte Carlo method falls in this category and was applied to AM processing [45, 46, 47, 48]. While the shape of the grains resulting from the competition between columnar and equiaxed grains were compared to experimental observations, the growth algorithm is not based on the physical mechanisms involved in the competition between dendritic branches. Moreover, the growth kinetics is not linked to the local supersaturation as in a classical model [49, 50, 51]. The cellular automaton method (CA) initially proposed in the early 90's [52, 53, 54] is most frequently used to deal with the simulation of the dendritic grain structure in AMed metallic alloys [22, 55, 56, 57, 58, 59, 60, 61, 62, 63, 64]. Initially developed for casting, it was extended to welding processing [65, 66] and benefited from optimized methodologies, including finite element (FE) mesh adaptation and parallel algorithms [67, 68], hence demonstrating the possibility to reproduce columnar grain structures and its associated texture in materials solidifying with cubic crystallography, i.e. with preferred growth direction of dendrites given by $\langle 100 \rangle$ crystallographic directions. The CA method was also recently compared with PF simulations to evaluate its ability to predict the grain boundary orientation of directionally solidified bicrystals, i.e. the basic mechanism leading to texture of columnar zones [69, 70]. This was only achieved in 2D due to limitations of the PF simulations. Recently adapted to additive manufacturing, the CA method was first applied to small domains (2D domains or single track) [55, 56], but used thereafter on larger domains to investigate multitrack multilayer constructions. Koepf *et al.* predict the grain structure of a IN718 part generated by L-PBF from an analytical Rosenthal temperature field [22]. Teferra and Rowenhorst use a more complex analytical solution and predict structures with different scanning strategies [64]. Finally, Zinovieva *et al.* link a FE resolution of the temperature field to a CA approach to obtain the microstructure on a larger domain [63].

This article presents a new methodology to model the grain structure generated in multitrack multilayer L-PBF constructions. The model is introduced in Sect. 2. The advantages of the new methodology are first discussed based on several single-track simulations in Sect. 3. Applications presented in Sect. 4 simulate REVs for regular manufacturing practices of parts made of the IN718 alloy. The influence of process parameters such as the laser power, the scanning strategy and the hatch spacing are demonstrated, as well as material parameters including the grain density of the substrate and the propensity to nucleate new grains in the melt pool. Results are compared considering the grain structure characterized by its texture, morphology and size. Sect. 5 concludes and elaborates on the possibility to reach a full part simulation rather than a REV as well as chaining of a virtual grain structure with other fields of

research.

2. Model description

The objective of the model is to compute the grain structure in a REV defined by a rectangular parallelepipedic block made of the IN718 alloy produced by L-PBF. The main directions of the block are aligned along the $(\mathbf{X}, \mathbf{Y}, \mathbf{Z})$ axes of a right handed Cartesian coordinate system. Layer by layer construction proceeds along the $\mathbf{Z}$ direction with a layer thickness t_l [m]. To construct each layer, the heat source of power P_{laser} [W] moves at constant velocity v_{laser} [$\mathrm{m \cdot s^{-1}}$] along linear tracks aligned with the $\mathbf{X}$ or $\mathbf{Y}$ directions or whichever direction is defined. The hatch spacing between linear tracks is denoted as h_s [m].

To model the grain structure of a REV, the local fusion and solidification of the metal is modeled by the transport of a stationary temperature field. A full thermohydraulic solution based on the FE method is presented in section 2.1. The CA method is summarized in section 2.2. The strategies to build a track shape and to transport the temperature field are then introduced in section 2.3.

2.1. Numerical and analytical solutions

Chen et al. have developed a numerical model to solve the thermohydraulic problem described by a free liquid-gas interface and solidification of materials with mushy zone applied to L-PBF [71, 72]. The energy (Eq. 1), the momentum (Eq. 2) and the total mass (Eq. 3) conservation equations are combined with a description of the free boundary between the ceramic material and the gas. The latter is modeled by a level-set function, ψ [m], which is a signed distance to the boundary with $\psi > 0$ in the gas and $\psi < 0$ in the material, thus localizing the boundary at position $\psi = 0$. The main originality of the model lies in the fact that mater not only denotes the dense material (substrate, consolidated layers, liquid) but also the porous material made of an equivalent powder bed medium with typically half the density of the dense material (50% porosity). This method avoids describing each powder particle and its interface. A compressible formulation enables to model the change of density due to melting of the powder bed by the laser. Queva et al. [73] adapted the model for metallic alloys by adding a recoil pressure force on the liquid-gas interface. A detailed description of the numerical thermohydraulic model and its solution using the FE method is given in Refs [71, 72, 73, 74]. It is therefore only briefly summarized hereafter. The system of equations writes as follows:

$$\frac{\partial \{\rho h\}}{\partial t} + \nabla \cdot \{\rho h \mathbf{u}\} - \nabla \cdot \{\lambda \nabla T\} = \left\{\dot{Q}\right\} \tag{1}$$

$$\{\rho\} \left(\frac{\partial \{\mathbf{u}\}}{\partial t} + (\{\mathbf{u}\} \cdot \nabla) \{\mathbf{u}\} \right) - \nabla \left\{\underline{\underline{\sigma}}\right\} = \{\mathbf{f_v}\} \tag{2}$$

$$\nabla \cdot \{\mathbf{u}\} = -\frac{1}{\{\rho\}} \frac{d\{\rho\}}{dt} \tag{3}$$

$$\frac{\partial \psi}{\partial t} + \mathbf{u}^{LS} \cdot \nabla \psi = 0 \tag{4}$$

with ρ [$\mathrm{kg \cdot m^{-3}}$] the density, h [$\mathrm{J \cdot kg^{-1}}$] the mass specific enthalpy, t [s] the time, λ [$\mathrm{W \cdot m^{-1} \cdot K^{-1}}$] the thermal conductivity, T [K or °C] the temperature and $\dot{Q}$ [$\mathrm{W \cdot m^{-3}}$] the heat supplied by the laser. Energy is transported in the melt pool by conduction and convection at velocity $\mathbf{u}$ [$\mathrm{m \cdot s^{-1}}$]. The liquid follows a compressible Newtonian behavior so the stress tensor $\underline{\underline{\sigma}}$ is linked to the strain rate tensor $\underline{\underline{\dot{\epsilon}}}$ through $\underline{\underline{\sigma}} = 2\mu\left(\underline{\underline{\dot{\epsilon}}} - \frac{1}{3} tr(\underline{\underline{\dot{\epsilon}}})\, \underline{\underline{\mathbf{I}}}\right) - p\mathbf{I}$ where $tr(\underline{\underline{\dot{\epsilon}}}) = \nabla \cdot \{\mathbf{u}\}$ is given by Eq. 3 with μ [$\mathrm{Pa \cdot s}$] the dynamic viscosity and p [Pa] the pressure. The displacement of the metal-gas boundary is computed by solving

the transport equation, Eq. 4, thus updating the position of the level-set function by using the computed velocity field $\mathbf{u}$. A smoothed level set function is defined, $\mathcal{H}(\psi) = \frac{1}{2}\big(1 + \frac{\psi}{\varepsilon} + \frac{1}{\pi}\sin(\frac{\pi\psi}{\varepsilon})\big)$ if $|\psi| \leq \varepsilon$, $\mathcal{H}(\psi) = 0$ if $\psi < -\varepsilon$ and $\mathcal{H}(\psi) = 1$ if $\psi > \varepsilon$, where ε is the half thickness of the boundary [71]. The latter is thus a numerical parameter that needs to be defined for a simulation. Averaging of quantity χ is defined by $\{\chi\} = \mathcal{H}(\psi)\chi^G + (1 - \mathcal{H}(\psi))\langle\chi^M\rangle$ with averaged properties in the metal, $\langle\chi^M\rangle$, and in the gas, χ^G. Additional volume averaging is applied to define the properties of the metal made of a mixture of n^ϕ [−] thermodynamic phases ϕ, hence notation $\langle\chi^M\rangle = \sum_{\phi=1}^{n^\phi} g^\phi\chi^\phi$ where g^ϕ [$\mathrm{m}^3 \cdot \mathrm{m}^{-3}$] is the volume fraction of phase ϕ with intrinsic phase properties χ^ϕ that depend on temperature.

The source term in Eq. 1 assumes a radial Gaussian distribution of the heat flux delivered by the laser, with standard deviation equal to half of the laser radius, r_{laser} [m]. The laser velocity is constant and its total power is partly transferred to the material with efficiency η [$\mathrm{W} \cdot \mathrm{W}^{-1}$]. The reflection, $(1-\eta)$, is established thanks to the formula proposed by Grange *et al.* [74]. Vaporization of the material at the surface of the melt is also accounted for [73]. It leads to a heat loss at the liquid-gas interface defined by the product of the vaporization rate, $\dot{m}$ [$\mathrm{kg} \cdot \mathrm{m}^{-2} \cdot \mathrm{s}^{-1}$], time the latent heat of vaporization, L_v [$\mathrm{J} \cdot \mathrm{kg}^{-1}$]. The vaporization rate is taken from literature and follows a Hertz-Langmuir-Knudsen law [75, 76]. As it is expressed per unit surface, the vaporization rate is transformed into a volumetric mass loss by multiplying it with the smoothed Dirac function, $\delta = \partial\mathcal{H}/\partial\psi$ [m^{-1}]. This procedure is inspired from the Continuum Surface Force (CSF) treatment [77] initially developed for surface tension. Finally, while the laser heat source is easily absorbed at the surface of the melt pool, scattering of the laser radiation between powder particles takes place due to partial absorption and reflections. Hence, an equivalent absorption coefficient, α [m^{-1}], is defined for the interaction within the powder bed of thickness t_p [m], assuming a Beer-Lambert's law along the laser Z trajectory [71]. Values of all material parameters are reported in Tab. 1 with distinction between powder, p, liquid, l, solid, s, and gas, g.

Similarly, the force acting in the right-hand-side of Eq. 2, $\mathbf{f_v}$ [$\mathrm{N} \cdot \mathrm{m}^{-3}$], is the sum of the surface tension, $(-\gamma\kappa\mathbf{n})$ with γ the surface energy [$\mathrm{J} \cdot \mathrm{m}^{-2}$] and $\kappa = \nabla \cdot \mathbf{n}$ the interface curvature defined by the divergence of the normal vector to the liquid-gas interface $\mathbf{n}$; plus the Marangoni force, $\big((\partial\gamma/\partial T)\nabla_S T\big)$ where ∇_S is the surface gradient operator; plus the recoil pressure [73]; plus the buoyancy force, $(\rho\mathbf{g})$ with $\mathbf{g}$ [$\mathrm{m} \cdot \mathrm{s}^{-2}$] the gravitational acceleration vector acting along the $-\mathbf{Z}$ direction. The forces applying on the liquid-gas surface are transformed to volumetric contributions by using the CSF methodology [77]. The temperature dependency of γ is taken as $\gamma = \gamma_L + (\partial\gamma/\partial T)(T - T_L)$; with coefficients listed in Tab. 1.

The solution of Eqs 1-4 is performed using the FE method. It is hereafter referred to as *numerical solution*. An adaptive mesh, called *FE mesh*, made of tetrahedral elements, is defined in order to maintain a sufficiently high spatial resolution at the frontier between the domains and to achieve convergence of the numerical solution. Typical outputs of the temperature field, the fluid velocity field in the melt pool and the metal-gas boundary, including the computed track shape, are presented in Fig. 1(a). The simulation considers a linear trajectory of the laser. With the chosen values of the velocity (Tab. 1) and power of the laser, a stable and stationary track is formed. It corresponds to stationary fields in the reference attached to the laser, i.e. fields that are simply translated at the velocity of the laser. This steady regime is checked by comparing over time the outputs of the simulation. More practically, the stability of the melt pool can be evaluated by the time evolution of the volume of the liquid metal, with a constant value expected for a steady regime, as well as constant height of the track.

Analytical solutions exist for a steady regime and are consequently convenient for comparison with numerical solutions. The heat flow problem is solved in a semi-infinite material domain assuming a horizontal and fixed material-gas interface and constant temperature at large distance from the heat source, T_0. Transport of energy only takes place by diffusion and the material is homogeneous, i.e.

assumes constant transport properties. The Rosenthal solution further assumes a point-like heat source of power ηP_{laser} [19]. Numerous grain structure simulations models are based on this approximation [22, 36, 78] as it provides with a simple mathematical expression of the temperature field according to the (x, y, z) coordinates attached to the heat source that moves at constant velocity v_{laser} on the material-gas surface, $z = 0$, in the x direction along a $y = 0$ line:

$$T(x, y, z) = T_0 + \frac{\eta P_{laser}}{2\pi\lambda r} \exp\left(-\frac{v_{laser}(x + r)}{2D}\right) \tag{5}$$

where $r = \sqrt{x^2 + y^2 + z^2}$ is the radial coordinate from the heat source, D and λ are the thermal diffusivity and the thermal conductivity of the material, respectively.

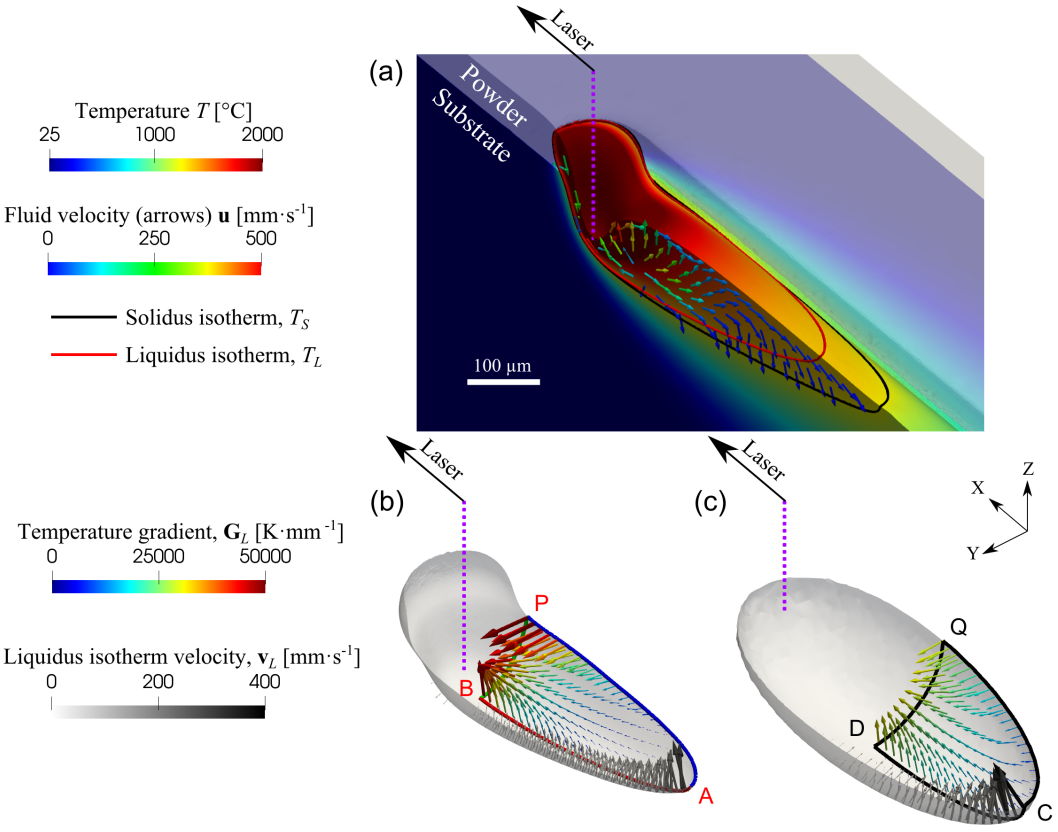

Figure 1: Steady 3D distributions of the temperature field, T, and the liquid velocity field, $\mathbf{u}$, for a single track formed by L-PBF of IN718. The temperature field is only represented at the surface of the metal, the gas being transparent and the powder translucent. The liquidus isotherm deduced from the numerical solution, (a, red contour) T_L, is used to extract (b) the lowest boundary of the melt pool, to be compared with (c) the corresponding field computed with the Rosenthal analytical solution. On these iso-surfaces are displayed (left, grey arrows) the liquidus isotherm velocity field, $\mathbf{v}_L$ and (right, colored arrows) the temperature gradient field, $\mathbf{G}_L$. Note that the density of the arrows in (a) and (b) are not representative of the FE mesh size. While the length of the arrows are constant in (a), they are adapted to the magnitude of the field in (b) and (c). Representation in (a) includes a longitudinal cut through the melt pool and the computed liquid metal velocity field, $\mathbf{u}$. Simulation parameters: Table 1 and laser power 120 W.

Fig. 1(b) and (c) present the liquidus isotherm surface predicted in the metallic domain after reaching steady state with the thermohydraulic numerical model and with the Rosenthal solution, respectively. As such, they give a representation of the liquid melt pool boundary underneath the metal-gas interface. For both simulations, the laser velocity and power are set to $v_{laser} = 400\,\mathrm{mm \cdot s^{-1}}$ and $P_{laser} = 120\,\mathrm{W}$ with efficiency $\eta = 61\%$; the far-field temperature (T_0 in Eq. 5) is maintained to 25 °C and properties similar to the one reported in earlier work are used [73], yet with constant values $D = 5.6 \times 10^{-6}\,\mathrm{m^2 \cdot s^{-1}}$ and $\lambda = 29\,\mathrm{W \cdot m^{-1} \cdot K^{-1}}$ for the Rosenthal equation. Values are reported in Tab. 1. The computed melt

	Parameter	Value	Unit	Parameter	Value	Unit
Material properties	ρ^p	3830	$\mathrm{kg \cdot m^{-3}}$	T_S	1240	°C
	ρ^s	7659	$\mathrm{kg \cdot m^{-3}}$	T_L	1337	°C
	ρ^l	7118	$\mathrm{kg \cdot m^{-3}}$	α^p	2×10^4	$\mathrm{m^{-1}}$
	ρ^g	1.3	$\mathrm{kg \cdot m^{-3}}$	α^s	2×10^4	$\mathrm{m^{-1}}$
	λ^p (T_0)	0.19	$\mathrm{W \cdot m^{-1} \cdot K^{-1}}$	α^l	1×10^5	$\mathrm{m^{-1}}$
	λ^s (T_0)	10.8	$\mathrm{W \cdot m^{-1} \cdot K^{-1}}$	α^g	0	$\mathrm{m^{-1}}$
	λ^l (T_L)	29.6	$\mathrm{W \cdot m^{-1} \cdot K^{-1}}$	μ^s (T_S)	1×10^3	$\mathrm{Pa \cdot s}$
	λ^g	2.4×10^{-2}	$\mathrm{W \cdot m^{-1} \cdot K^{-1}}$	μ^p, μ^l (T_L)	3×10^{-2}	$\mathrm{Pa \cdot s}$
	c_p^l	754	$\mathrm{J \cdot kg^{-1} \cdot K^{-1}}$	μ^g	2.4×10^{-2}	$\mathrm{Pa \cdot s}$
	c_p^s	643	$\mathrm{J \cdot kg^{-1} \cdot K^{-1}}$	L_v	6.69×10^6	$\mathrm{J \cdot kg^{-1}}$
	c_p^g	1000	$\mathrm{J \cdot kg^{-1} \cdot K^{-1}}$	$\|\mathbf{g}\|$	9.81	$\mathrm{m \cdot s^{-1}}$
	$(\partial\gamma/\partial T)$	-1×10^{-4}	$\mathrm{J \cdot m^{-2} \cdot K^{-1}}$	γ_L	1.7	$\mathrm{J \cdot m^{-2}}$
Rosenthal	λ	29.6	$\mathrm{W \cdot m^{-1} \cdot K^{-1}}$	D	5.6×10^{-6}	$\mathrm{m^2 \cdot s^{-1}}$
Process properties	v_{laser}	400	$\mathrm{mm \cdot s^{-1}}$	r_{laser}	35	µm
	η	0.61	-	τ	2.5×10^{-4}	s
	T_0	25	°C	t_p	50	µm
FE parameters	ε	10	µm	h_{FE}^{min}	0.5	µm
	Δt	3×10^{-6}	s			
CA parameters	n_S	3×10^4	$\mathrm{mm^{-3}}$	h_{CA}	10	µm
	A	1.85×10^{-7}	$\mathrm{m \cdot s^{-1} \cdot K^{-n}}$	l_{CA} (ST)	2	µm
	n	3.66	-	l_{CA} (REV)	1.5	µm
	ΔT_n^μ	0	K	ΔT_n^σ	0	K

Table 1: Common process, material and numerical parameters for ST simulations cases listed in Tab. 2.

pool dimensions (length/width/depth) are (346/104/65) µm and (345/152/76) µm for the numerical and analytical solutions, respectively, the depth being defined by the difference in Z coordinate between the top surface of the substrate, labelled P and Q in Fig. 1, and the lowest point of the melt pools, labelled B and D in Fig. 1. At each point of the liquidus isotherm surface, analysis of the heat flow provides with the temperature gradient, $\mathbf{G}_L = G_L \cdot \mathbf{n}_L$, and the velocity, $\mathbf{v}_L = v_L \cdot \mathbf{n}_L$, where $\mathbf{n}_L$ is the local normal to the surface. With a constant laser velocity, $\mathbf{v}_{laser}$, the magnitude of the isotherm velocity is given by $v_L = \mathbf{v}_{laser} \cdot \mathbf{n}_L$. As explained in the introduction, these data are of interest for analyzing the microstructure formation within the mushy zone [2]. Results are plotted using arrows in Fig.1(b) and (c).

It is then possible to draw profiles of temperature gradient versus isotherm velocity starting from the top-rear position labelled (b) A and (c) C, following the bottom of the pool to reach the lowest position (b) B and (c) D, and forming a closed contour by going up along the side of the melt pool to position (b) P and (c) Q and back to the initial position while remaining at the surface between the metal and the gas, defined by (numerical) $\psi = 0$ and (analytical) $z = 0$. These profiles are drawn in Fig. 2 for the numerical and analytical solutions while using the same color code for the contours in Fig.1(b) and (c). Results show that the range of velocities along the lower boundary of the melt pool is almost the same for both models. Nevertheless negatives values are observed for the numerical solution, mainly along the green line drawn in Fig.1(b), that corresponds to local remelting (the isotherm velocity does not progress in the direction of the melt pool but in the direction of the solid material). Such observation is expected in the front part of the melt pool where remelting by the laser heat source takes place. One can also observe that the liquidus isotherm velocity at the top rear part of the melt pool is equal to the laser velocity for the analytical solution, i.e. at point C in Fig.1(c). This is a well known property of the Rosenthal solution, also corresponding to a normal vector to the liquidus isotherm (or direction of the temperature gradient) aligned with the scanning direction of the laser. It differs from the numerical solution as velocity at position A in Fig.1(b) is reduced and the temperature gradient is no longer aligned

with the laser velocity. Fig. 2 also reveals that the range of temperature gradient is very different. For both models, the highest temperature gradients are located in the transverse sections at the deepest position of the melt pool where numerical and analytical solutions take similar values. The temperature gradient then decreases toward the back of the melt pool but around 50 times less for the Rosenthal solution compared to the computed thermohydraulic numerical solution. It can also be noticed that all 3 contours deduced from the analytical solution form a single path (two black lines are superimposed and the third one reduced to a single point) while the red and blue lines are well distinguished for the numerical model with lower temperature gradient along the $z = 0$ contour defined by the boundary between the powder and the dense metal.

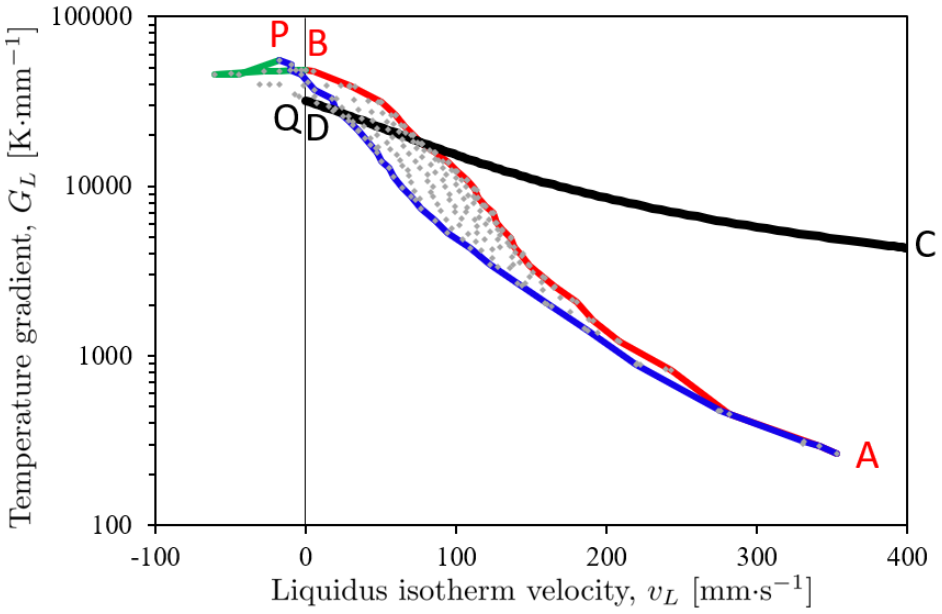

Figure 2: Temperature gradient versus velocity of the isotherm along the lines drawn on the liquidus surface for (Fig. 1b) the numerical model and (Fig. 1c) the analytical Rosenthal solution. Colors of the curves and labels A-D correspond to the one used in Fig. 1.

2.2. Cellular Automaton method

To model the grain structure, a cellular automaton grid is defined. It is made of a regular lattice of cubic cells with homogeneous size, l_{CA}, referred to as *CA grid*. A methodology is applied to access to computed fields in the vicinity of each cell using the solutions of the heat flow described in Section 2.1, mainly *i*- the temperature, either using the numerical solution or the analytical Rosenthal solution, and *ii*- the position of the cell with respect to the evolving metal-gas boundary, simply informing if it falls in the gas or in the dense metallic domain (see Sect. 2.3). Because detailed description of the CA method is already made available in the literature [53, 54, 65, 67, 69, 70, 66], only its principles are reminded in the present section.

Each CA cell is attributed with an index that describes its state chosen among *gas*, *liquid*, *mushy* or *solid*, the last three states corresponding to the metallic subdomain. Rules are defined to switch the cell index from one state to another, and hence to model the evolution of the metal-gas interface and melting/solidification. Simulation starts from a substrate with initial grain density, n_S [m^{-3}]. This means that a grain structure already exists in the lower part of the CA grid that contains dense solid metal (i.e., the substrate or consolidated material), the rest of the grid being initially assimilated to gas cells. A grain is made of contiguous cells sharing a unique crystallographic orientation defined by a triplet of Euler angles $(\varphi_1, \Phi, \varphi_2)$ in the Bunge convention [79]. Upon reaching a temperature above T_L, solid cells

are switched to liquid cells by changing their state index. The state index of the cells with temperature below T_L and with at least one liquid neighbouring cell is switched to mushy. Mushy cells are attributed with an octahedron of small initial size ($l_{CA}/1000$) centered with the cell [54]. The main directions of the octahedron coincide with the $\langle 100 \rangle$ crystallographic directions of the grain to which the cell belongs. They represent the directions of the dendrite branches in cubic systems. Integration over time of a dendrite tip growth kinetics is performed to increase the size of the half-diagonals of the octahedron and hence to grow the microstructure. When the octahedron encompass the center of a neighboring liquid cell, the latter is itself switched to a mushy state and inherits from the same crystallographic orientation as the capturing cell, thus propagating the grain. The methodology to initialize the octahedron of the newly captured cell is described elsewhere [54]. If no liquid cell remains in the vicinity of a mushy cell, its growth is stopped and the cell is switched to a solid state.

The dendrite tip growth kinetics is computed using the model developed by Kurz *et al.* [49], extended to multicomponent alloys by Hunziker [50] and coupled with thermodynamic and mobility databases [80] by Guillemot *et al.* [51, 81]. The velocity of the dendrite tip, v_t, is related to its undercooling, $\Delta T_d = T_L - T_d$ [K], where T_d [K] is the temperature at the dendrite tip. The tetrahedral element of the mesh containing the apex of the octahedron is found. Its node temperatures are used to compute the tip temperature and then the undercooling. The $v_t(\Delta T)$ relationship is approximated by a power law. For IN718, the use of the dedicated Ni-based superalloy TCNI10 [82] and MOBNI5 [83] leads to the relationship $v_t = A\,\Delta T_d^n$ with $A = 1.85 \times 10^{-7}\,\mathrm{m \cdot s^{-1} \cdot K^{-n}}$ and $n = 3.66$.

In some simulations, nucleation of new grains in the melt is also modeled. For that purpose, nucleation sites are randomly distributed among the cells of the CA grid with a prescribed nucleation undercooling, ΔT_n [K], following a gaussian distribution parameterized by the maximum nucleation density, n_V [$\mathrm{m^{-3}}$], a mean undercooling, ΔT_n^μ [K], and a standard deviation, ΔT_n^σ [K]. If the temperature of a liquid cell containing the nucleation site to be activated at undercooling ΔT_n falls below $T_L - \Delta T_n$, a new grain is formed by switching the cell index from liquid to mushy. It is then assigned with a randomly selected triplet of Euler angles and the same initialization explained previously for mushy cells is performed, including the creation and localization of an octahedron of small initial size ($l_{CA}/1000$) centered with the cell.

Fig. 3 shows a typical snapshot of the longitudinal cross-section of the CA grid during a simulation when reaching a steady regime. It makes use of the thermohydraulic solution shown in Fig. 1, revealing the powder thickness in front of the laser, the effect of the recoil pressure and all forces on the shape of the liquid/gas interface and the consolidated height of the layer after solidification. Cells above T_L are liquid and appear in grey. With the gas and powder cells in white, they delimit the melt pool boundary, also greatly corresponding to the level-set isosurface $\psi = 0\,\mathrm{m}$. Below T_L, the liquid cells are undercooled. Nucleation of new grains in the undercooled liquid is shown by colored cells surrounded by grey cells, with a color defined by the value of the first Euler angle of the corresponding grain orientation. The colored cells at the boundary with the grey cells are in a mushy state, meaning that they can grow and capture neighbouring liquid cells. The colored cells fully surrounded by other colored cells take the solid state index. One can visualize in the right-hand-part of the figure the initial grain density of the substrate that is not yet remelted, n_S. The difference between the height in front of the laser and at the rear of the track is the maximum consolidated thickness of the construction layer. The modification of the grain structure due to melting/solidification is clearly visible.

2.3. Track shape and temperature field

The numerical model can be chained to the CA method to simulate the grain structure generated by the laser path alongside with the thermohydraulic solution (e.g., Figs 1 and 3). However, due to the high computing resources required, this approach is restricted to a single track and can hardly be used to

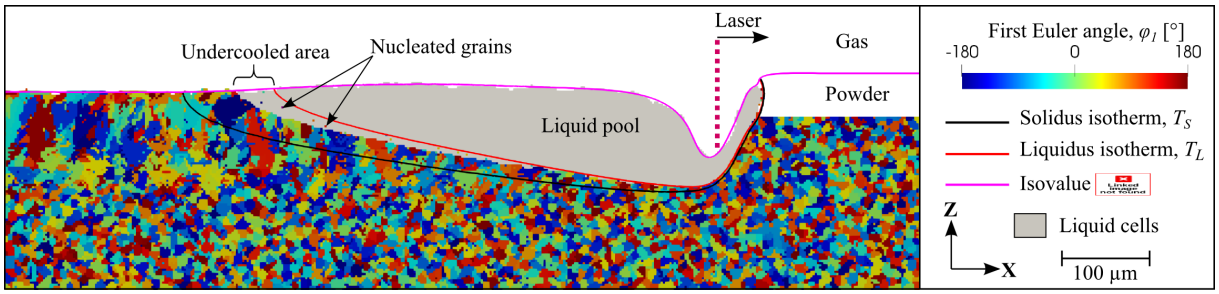

Figure 3: Snapshot of a cross-section through a linear laser track of the CA grid colored using the first Euler angle φ_1 of the grains and grey and white colors for the liquid and gas/powder subdomains, respectively. The magenta line outlines the position of the material/gas boundary resulting from the cross section of the 3D isosurface of the level-set function $\psi = 0\,\mathrm{m}$.

simulate the grain structure of a REV. We hereafter present the methodologies used to circumvent this limitation.

The FE mesh is adapted during a FE simulation while the CA grid is made of fixed CA cells. Exchange of information between the two models thus requires to update the localization of the cells within the FE mesh at each time remeshing takes place. This procedure was initially implemented [67] but found inefficient for 3D simulations. Instead, the procedure developed for welding simulations is used [65, 66]. It is based on an intermediate finite element mesh, called *CA mesh*, defined on top of the FE mesh, but made of fixed tessellation and a homogeneous mesh size, h_{CA}, with $h_{CA} > l_{CA}$. As both the CA mesh and the CA grid are fixed, a unique connectivity between the elements and the cells is initialized at the beginning of a simulation. Only the information at CA mesh is updated at each time of a simulation by the transport of the information from the adapted FE mesh, which is much more efficient.

Three combinations of the temperature field and metal-gas boundary are considered for simulations of the grain structures:

- $\mathrm{M^{FE}}$. The results of the numerical model are directly transported from the FE mesh to the CA grid (via the CA mesh) and used to apply the CA model for grain structure simulation. This is the common methodology developed for welding and explained in details elsewhere [65, 66]. It means that, at each time step of the numerical model, the position of the metal-gas boundary and the temperature field are made available at the level of the CA cells. The grain structure simulation then becomes an add-on module to the numerical thermohydraulic simulation, including non-stationary evolution of all fields. Fig. 3 gives an illustration of this approach.

- $\mathrm{H^{FE}}$. This hybrid combination starts from the steady regime of the numerical simulation deduced from the thermohydraulic numerical model, when a constant volume of the melt pool and a constant track shape is reached, the temperature and liquid velocity fields being simply translated at the velocity of the laser. A parallelepipedic box, illustrated by the black contours in Fig. 4($\mathrm{M^{FE}}$), is defined. It contains both the melt and the mushy zone, i.e. also including the final profile of the consolidated track made of melted and resolidified powder in the aftermath of the laser. The position and orientation of the box are defined with respect to the laser heat source and the powder bed. Within the box, the shape of the top part of the consolidated track is extracted from the transverse section behind the laser position, at a temperature below T_S. In Fig. 4($\mathrm{H^{FE}}$), it corresponds to the green dotted contour defining the basis of a prism in a **YZ** section deduced from the lowest X position of the black box defined in Fig. 4($\mathrm{M^{FE}}$). A distance function φ^{FE} is further defined on the CA mesh. It is the signed distance to the metal-gas boundary. In this approach, the powder is assimilated to gas and the metal is located in the region $\varphi^{FE} < 0$. This function is initialized as $\varphi^{FE} = Z - Z_{top}$, the substrate top surface being at constant horizontal position $Z = Z_{top}$. At each time-step Δt, the length of the prism along the scanning direction of the laser is $v_{laser} \cdot \Delta t$. The

signed distance d_p to the prism is computed at each node of the CA mesh with negative values inside the prism and positive outside. Updating of φ^{FE} is then carried out by assigning the minimum of its current value and the signed distance d_p. The gas cells undergoing a variation from $\varphi^{FE} > 0$ to $\varphi^{FE} < 0$ are finally switched to liquid cells to mimic the construction of the track. The 3D temperature field deduced from the numerical model, T^{FE} is recorded within the box with high spacial resolution (5 µm spacing was typically used for the present simulations) and can then be interpolated to the CA mesh, as shown in Fig. 4($\mathrm{H^{FE}}$). The box, including the consolidated metal construction and the 3D temperature field attached to the laser are then translated to follow the scanning strategy. This is referred to as the hybrid FE solution, $\mathrm{H^{FE}} = \mathrm{H}(\varphi^{FE}, T^{FE})$.

- $\mathrm{H^{Ros}}$. Using the analytical Rosenthal solution, the shape of the track is not defined. It is hereafter simply assimilated to a brick shape positioned on top of the initial metal-powder boundary as shown in Fig. 4($\mathrm{H^{Ros}}$). The height of the rectangular section of the brick, h_t, corresponds to the consolidated layer thickness or piston increment, t_l. An arbitrary width is chosen, of the order of the melt pool width, w_m. As for the previous methods, the length of the brick is given by $v_{laser} \cdot \Delta t$. A distance function φ^{Ros} is initialized on the CA mesh by $\varphi^{Ros} = Z - Z_{top}$. At each time-step, the distance d_b to the brick is computed and the value of φ^{Ros} is updated using the minimum between the current values of φ^{Ros} and d_b. The sign function $\varphi^{Ros} < 0$ localizes the metal and the temperature field, T^{Ros}, is computed using Eq. 5 when knowing the position of the laser $(X_{laser}, Y_{laser}, Z_{laser})$. Note that Z_{laser} is located at the top surface of the track. This is referred to as the hybrid Rosenthal solution, $\mathrm{H^{Ros}} = \mathrm{H}(\varphi^{Ros}, T^{Ros})$.

Hence, in the case of the hybrid methodologies, $\mathrm{H^{FE}}$ and $\mathrm{H^{Ros}}$, both the prescribed sign function and the temperature field are interpolated to the CA mesh in a reference frame attached to the laser and are directly used for the computation of the grain structure. In other words, no thermohydraulic numerical solution needs to be computed, considerably decreasing the required computational resources compared to the full numerical $\mathrm{M^{FE}}$ methodology. It should be noticed that, because the start (end) of the linear trajectories are not made accessible by the hybrid methodologies, the temperature is progressively increased (resp. decreased) from an initial value T_0 up to the steady state temperature during a transition time τ. The actual temperature T applied to the CA mesh (and then to the CA cells) is $T = T_0 + (T^* - T_0)t_s/\tau$ if $t_s < \tau$; $T = T_0 + (T^* - T_0)(t_f - t_s)/\tau$ if $t_f - t_s < \tau$; and $T = T^*$ otherwise, where t_s is the time spent since the beginning of the scan, t_f is the final scanning time of one track, and T^* is T^{FE} or T^{Ros}. Thereby, the temperature does not drastically increase/drop at the start/end of a scan. It is progressively modified. This simple procedure to handle transient heat flow regimes prevents from reaching very high undercooling. In the following, however, the transient zones are not accounted for when performing the grain structure analyses.

3. Single track simulations

The first category of simulations aims at analyzing the influence of the hybrid methodology on the generated grain structure. All cases are run in a domain of length 1.5 mm, width 0.5 mm and height 1.1 mm. The substrate is 0.95 mm thick and the overlaid powder layer is 50 µm thick. A 1 mm long single track (ST) is considered with the $\mathrm{M^{FE}}$ methodology, referred to as case #A. The trajectory of the laser starts at $X = 0.25$ mm and ends at $X = 1.25$ mm, while maintaining the Y coordinate constant, at mid-width of the domain. This ST length was found sufficient to reach a steady regime with the thermohydraulic numerical model, as defined in Sect. 2 and illustrated in Figs 1-4. It thus serves as input to build the corresponding $\mathrm{H^{FE}}$ hybrid methodology using the same value of the laser power, $P_{laser} = 120$ W. This case is referred to as ST #B. A second comparison using the same power of the

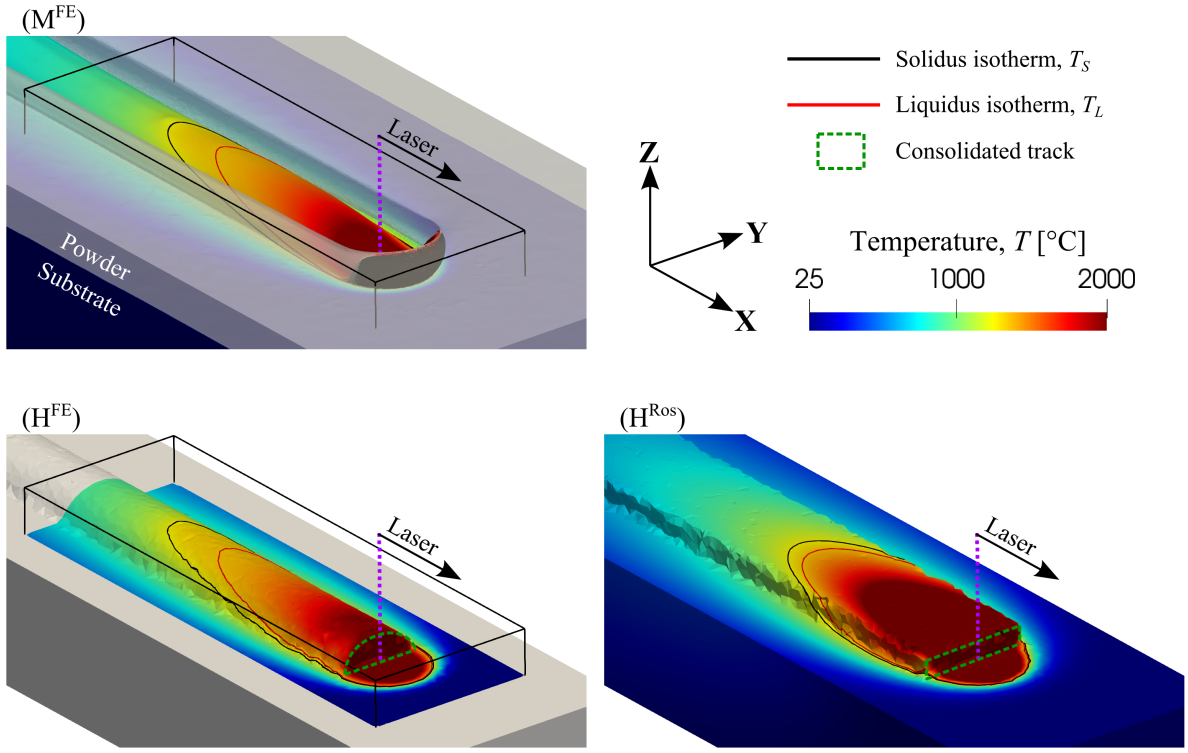

Figure 4: Steady temperature and track shape obtained with (M^{FE}) the full numerical thermohydaulic model visualized using the FE mesh, (H^{FE}) the hybrid methodology using the temperature field stored in the black box shown in M^{FE} and applied onto the CA mesh, with track shape extruded up to the laser position using its final section shape deduced from M^{FE}, and (H^{Ros}) the hybrid methodology using the Rosenthal temperature field applied to the CA mesh with a track shape approximated by a brick with height defined by the consolidated layer thickness deduced from M^{FE}.

laser but making use of the analytical solution, H^{Ros}, is denoted case ST #C. Finally, the role of the laser power is also studied, decreasing its value to $P_{laser} = 80\,\mathrm{W}$ for case ST #D. All cases are listed in Tab. 2.

For all simulations, the velocity of the laser heat source is maintained at $v_{laser} = 400\,\mathrm{mm \cdot s^{-1}}$ and the external temperature is kept at $T_0 = 25\,^{\circ}\mathrm{C}$. A Gaussian distribution of the heat source is used with radius $r_{laser} = 35\,\mu\mathrm{m}$ for the numerical model. Grain nucleation in the undercooled liquid melt is not considered. This is achieved by setting $n_V = 0\,\mathrm{mm^{-3}}$. The same initial substrate microstructure was also used in all cases, with density $n_S = 3 \times 10^4\,\mathrm{mm^{-3}}$ and random crystallographic orientation of the grains. All simulation parameters are listed in Tab. 1.

While maintaining a constant laser power and making use of the thermohydraulic numerical model, the grain structure is either (#A) directly computed as part of the full non-stationary temperature field or (#B) deduced from the stationary consolidated track shape and the temperature field stored in a box and moved with the laser. The fully solidified microstructures are made accessible in Fig. 5(#A) and (#B) for comparison of methodologies M^{FE} and H^{FE}. Focusing on the central zone of case #A, denoted "steady", the height of the consolidated track is almost constant. The grain structures are found to be very similar in the central zone. Most of the grains grew epitaxially from the partially remelted substrate and propagated up to the top of the track, i.e. in the direction $\mathbf{G}_L$. During growth, Figs 1 and 3 show that $\mathbf{G}_L$ progressively decreases in intensity and tilt from the initially $+\mathbf{Z}$ direction to around 10° off in the $+\mathbf{X}$ direction of the laser. This is also observed on the grain structure. The transverse cross section at the center of the track (cut at coordinate $X = 0.75\,\mathrm{mm}$) confirms this observation and also reveals the good reproduction of the track shape. Only small differences are observed considering the size and shape of the grains. The initial and final transient zones reveal track heights that differ from the steady

zone in case #A, while it is imposed constant in case #B. This was expected as morphology of the melt pool did change with time in the transient zones of case #A. The color map used to draw the grain structure is based on the inverse pole figure considering the **Y** axis. In this simulation, only very few grains are eliminated due to growth competition among columnar dendritic grains. This is not surprising considering the fact that the melt pool only contains few grains due to the relatively coarse initial grain structure of the substrate. Consequently, studying the texture formation during directional growth while using the same grains density n_S requires a larger domain size in the vertical building direction, hence the REV constructions in the next section.

Always with the same laser power, case #C is based on methodology $\mathrm{H^{Ros}}$. The melt pool dimensions are given in Tab. 2 as the length, l_m, the depth, d_m, and the width, w_m, as well as the final track height, h_t. While values are obviously the same for cases #A and #B, they significantly differ for case #C mainly due to the different temperature fields shown in Fig. 2 and 4. The grain structure is clearly influenced, with more elongated shapes in the laser direction when reaching the upper part of the track. This is of course due to the analytical solution that leads to a temperature gradient exactly aligned with the $+\mathbf{X}$ axis at the top rear of the melt pool, i.e. in the same direction as the laser heat source moves. Hence, the preferred selected $\langle 100 \rangle$ dendrite growth direction changes from well aligned with the $+\mathbf{Z}$ direction at the bottom of the melt to well aligned with the $+\mathbf{X}$ direction at the top of the melt. It is worth noticing that the shape of the 2D cross sections in Fig. 5 is of course also very approximate compared with the reference solution case #A or its simplified case #B.

The last case consider a change in the process parameters, with a 1/3 decrease of the laser power. Result of case ST #D is to be compared with case ST #A as they share the $\mathrm{M^{FE}}$ methodology. The evolution of the dimensions of the melt pool are in good agreements with the reported effect of linear energy decrease, P_{laser}/v_{laser} [71, 73]. With a more inclined temperature gradient in the upper part of the melt, columnar growth is more tilted in the $+\mathbf{X}$ direction.

Simulation times are also informed in Tab. 2. All cases were run on 28 processors. While case ST #A and #D required more than 7 days, cases ST #B and #C only lasted around 40 minutes. The reason is of course that no FE resolution is needed in the hybrid methodologies that only consist of the CA calculation, reaching similar times for all cases. In fact, beside the CA grain structure simulations, the time associated to the hybrid methodologies are only due to the projection of (#B) the 3D stationary temperature field stored in the box and projected onto the CA mesh and (#C) the computation of the temperature field at the nodes of the CA mesh by using Eq. 5. Several conclusions can be drawn from these observations:

- Despite its simulation time, the standard $\mathrm{M^{FE}}$ method is not sustainable for modeling the grain structure at a part scale or for a REV of an AMed component using multitrack multilayer strategies.
- The hybrid methodology $\mathrm{H^{FE}}$ can advantageously be exploited if one accept to approximate the consolidated track shape and temperature fields required for grain structure simulations by the stored outputs of a previously established steady solution of the full thermohydraulic numerical simulation, e.g. using outputs of the simulation reported in Fig. 4(a) on a FE mesh and projected in a small window on a coarser CA mesh as in Fig. 4(b).
- The hybrid methodology $\mathrm{H^{Ros}}$ is too simplistic to well represent the grain structure. This is due not only to the absence of a track shape predicted by the analytical solution but also to the approximations when establishing the temperature field (no convection, point-like heat source, constant thermophysical properties, ...).

Considering the difference between the computation times of the two hybrid solutions, there is no reason to favor an analytical solution. Consequently, the $\mathrm{H^{FE}}$ methodology will be largely favored hereafter.

ST case	P_{laser} [W]	Method	l_m [µm]	w_m [µm]	d_m [µm]	h_t [µm]	Simulation time CA[min]	FE[min]
#A	120	M^{FE}	346	106	66	33	44	9652
#B	120	H^{FE}	346	106	66	33	37	6
#C	120	H^{Ros}	345	152	51	25	37	5
#D	80	M^{FE}	293	94	45	34	38	10 026

Table 2: Parameters for the 1 mm long single track (ST) simulation cases #A to #D reported in Fig. 5, characterized by the power of the laser, P_{laser}, and the method used to compute the temperature field. The list of the common parameters is given in Tab. 1. The output dimensions of the steady melt pool are reported, including the length, l_m, the depth, d_m, and the width, w_m, as well as the final track height, h_t.

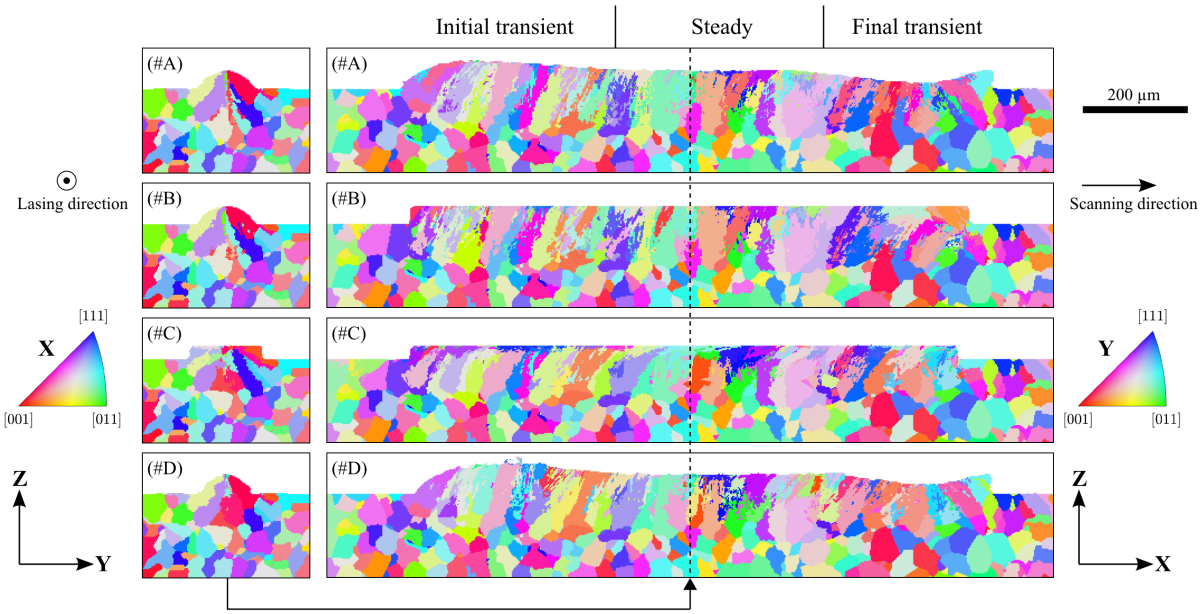

Figure 5: IPF maps of the grain structure as observed in cross-sections (left) perpendicular and at mid-way of the laser trajectory, i.e. central transverse plane defined by the **YZ** cut at $X = 0.75$ mm and (right) along the path of the laser, i.e. central longitudinal plane defined by the **XZ** cut at $Y = 0.25$ mm, for ST simulations #A-#D reported in Table 2.

4. REV simulations

The second category of simulations aims at computing the grain structure in a representative elementary volume (REV) of an AMed component by performing multitrack multilayer constructions. All simulations are based on the hybrid H^{FE} methodology deduced from the M^{FE} ST simulations reaching steady state, #A and #D, except one based on the hybrid H^{Ros} methodology, #C. Tab. 3 lists all REV simulations, numbered from #1 to #12, and its corresponding ST basis. Case REV #1 serves as reference. Its results are first described into details considering IPF grain structure maps as well as statistical analyses. The effects of process parameters (scanning strategy, hatch spacing and laser power) and nucleation parameters (initial grain density of the substrate and nucleation of new grains in the undercooled melt) are then successively studied, with modified parameters reported in Tab. 3.

For all simulations, a parallelepipedic block with section $600 \times 600\,\mu m^2$ is used. Construction takes place along the $+\mathbf{Z}$ direction on a 100 µm thick substrate with an initial metal domain identified by the distance function $\varphi^{FE} < 0$ (or $\varphi^{Ros} < 0$). The function is initialized with a trivial expression, $\varphi^{FE} = \varphi^{Ros} = Z$, the substrate lowest and highest positions being respectively at coordinate $Z = -100\,\mu m$ and $Z = 0\,\mu m$. At each new track, the φ^{FE} (or φ^{Ros}) function is updated to always represent the consolidated metal-gas boundary, such as described in part 2.3. The consolidated track shape and temperature fields are interpolated on the CA mesh of homogeneous size $h_{CA} = 10\,\mu m$ (i.e., same values as for ST simulations

reported in Sect. 3 Tab. 1.) A total of 40 layers of thickness $t_l = 25\,\mu\text{m}$ makes a 1 mm height rectangular block above the initial top surface of the substrate. The powder porosity is estimated at 50%. At a steady state of the construction, the thickness of the deposited powder layer is twice the thickness of added mater at each layer. The latter being equal to the piston increment t_l, the powder layer thickness used in the models is $t_p = 2 \cdot t_l$. Each layer contains 8 adjacent tracks, yet increased to 10 for case REV #2 that uses a smaller hatch spacing and increased to 12 for case REV #6 based on scanning directions misaligned with the edges of the block section. For all simulations, the CA cell size is set to $l_{CA} = 1.5\,\mu\text{m}$, the block requiring around 120 millions cells. The various nucleation parameters, n_S and n_V, are listed in Tab. 3. One can notice that the effect of no nucleation in the melt, $n_V = 0\,\text{mm}^{-3}$, and a single crystal substrate are also part of the simulations, i.e. REV cases #9-#12.

Three scanning strategies are used. They are based on linear trajectories of the laser on the top surface of the block to built adjacent tracks in each layer. The following denomination is used, with the origin of the O**XYZ** frame of reference shown in Fig. 6:

- S_L^X: opposite bidirectional monoaxial scanning. In each layer, starting from position ($X = 0\,\text{mm}$, $Y = 0.035\,\text{mm}$) for all cases but REV #2 using ($X = 0\,\text{mm}$, $Y = 0.075\,\text{mm}$), the laser scans the surface with trajectories parallel to X edges of the block. It alternates between the $+\mathbf{X}$ and $-\mathbf{X}$ directions for odd and even scans, respectively. At the end of each linear scan of length 0.750 mm, the Y coordinate is increased by the hatch spacing, h_s, reaching $Y = 0.567\,\text{mm}$ with the last (8^{th}) scan within the same layer ($Y = 0.525\,\text{mm}$ for the 10^{th} scan for REV #2). At the next layer, the same strategy is performed. This is illustrated in Fig. 6(S_L^X). It is worth noting that the linear path defined for each scan is longer than the section edge. While the initial position of the laser starts at the edge of the 0.600 mm length of the domain, its final position falls outside the simulation domain. This is organized so that the melt pool is not present at the end of a linear scan but progressively leaves the simulation domain. This ensures smoothed and steady melting and solidification for each trajectory in a time stepping procedure.

- S_L^{XY}: opposite bidirectional orthogonal biaxial scanning. The same strategy as S_L^X is applied to odd layers. For even layers, the strategy starts from the initial coordinate ($X = 0.035\,\text{mm}$, $Y = 0\,\text{mm}$). Scanning is performed parallel to the Y edges, along the $+\mathbf{Y}$ and $-\mathbf{Y}$ directions for odd and even scans, respectively, while the laser is moved by h_s along the $+\mathbf{X}$ direction at the end of each linear scan. This strategy is illustrated in Fig. 6(S_L^{XY}).

- S_L^{67}: opposition bidirectional 67° rotation multiaxial scanning. After a first scan equivalent to S_L^X for the first layer, a 67° rotation of the scanning strategy is applied for the next layers around an axis centered with the block section and directed in the $+\mathbf{Z}$ direction. It defines a new axis in the XY section for the opposite bidirectional linear scanning of the second layer as illustrated in Fig. 6 (S_L^{67}). The 67° rotation is applied at each new layer. Note that the number of scan per layer is increased to 12, the length of individual scan is increased to 850 µm and the initial position of the first scan is adjusted to ($X = -0.125\,\text{mm}$, $Y = -0.116\,\text{mm}$) so as to ensure a full rectangular scan of the block section for all the layers.

4.1. Reference case

At first, it is worth saying that the present REV simulations could only be achieved with the hybrid methodologies. Indeed, reference case #1, shown in Fig. 7, requires more than 10 days of computation time while using optimized parallel algorithms for the CA model [68] over 28 processors. With 40 layers, each one made of 8 individual 750 µm long linear scans, the total trajectory length reaches 240 mm. If one considers a typical value of $40\,\text{min} \cdot \text{mm}^{-1}$ over 28 processors, as suggested by the hybrid ST cases (Tab.

REV case	ST case	Scan	h_s [µm]	n_S [mm^{-3}]	n_V [mm^{-3}]	Figures
#1	#B	S_L^X	76	$3 \cdot 10^4$	10^7	7, 8, 9, 10, 12, 13
#2	#B	S_L^X	50			8, 9, 10
#3	#D*	S_L^X	76			8, 9, 10
#4	#C	S_L^X	76			8, 9, 10
#5	#B	S_L^{XY}	76			8, 11, 12
#6	#B	S_L^{67}	76			8, 11, 12
#7	#B	S_L^X	76	$3 \cdot 10^4$	10^6	12, 13
#8	#B	S_L^{XY}		$3 \cdot 10^4$	10^6	12
#9	#B	S_L^X		$3 \cdot 10^4$	0	11, 12, 13
#10	#B	S_L^{XY}		$3 \cdot 10^4$	0	11, 12
#11	#B	S_L^X		SC	10^7	13
#12	#B	S_L^X		10^7	0	13

Table 3: Parameters for representative elementary volume (REV) simulation cases #1 to #12 reported in Figs 7-13, characterized by the ST case (Tab. 2), the grain density in the substrate, n_S, and the density of potent nucleation sites in the liquid, n_V, the hatch spacing, h_s, the scanning strategy of the laser heat source (Fig. 6). For each case, the text in red highlights the difference with the reference case #1. SC: single crystal substrate, with Euler angles corresponding to ⟨100⟩ crystallographic directions aligned with the axes of the reference frame. #D* refers to the use of the H$^{\mathrm{FE}}$ strategy with the ST #D process properties.

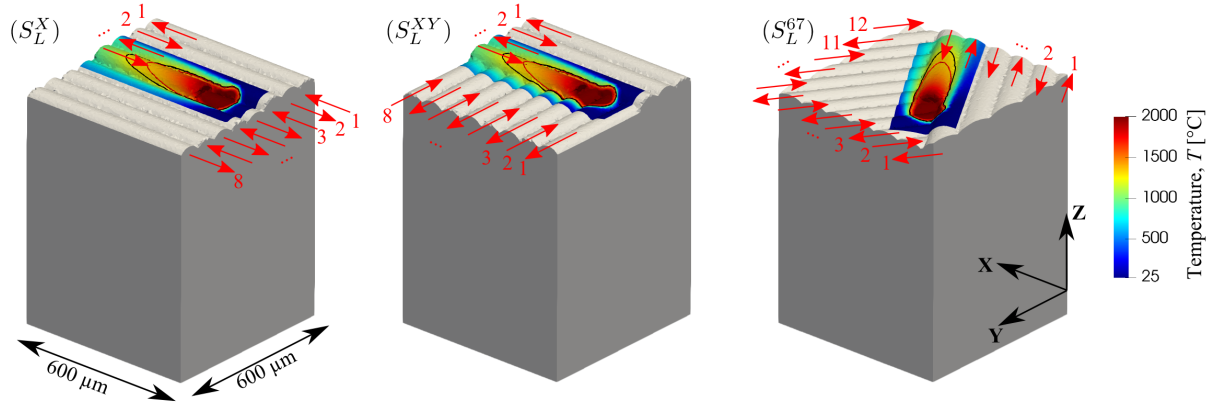

Figure 6: Global view of the REV under fabrication with the hybrid H$^{\mathrm{FE}}$ temperature field corresponding to Tab. 2 ST case #B (also REV cases #1-#2 and #5-#12). Only part of the domains made of 40 consolidated material layers is shown, i.e. corresponding to $Z_M < 0$ at the time of the fabrication. Detailed description of (S_L^X) the bidirectional scanning strategy applied to all layers (Tab. 3 REV cases #1-#4, #7, #9, #11-#12), its extension including (S_L^{XY}) a ±90° shift across the next layer (Tab. 3 REV cases #5, #8, #10) and (S_L^{67}) a 67° shift across the next layer (Tab. 3 REV case #6) are explained in detail in the main text.

2), this leads to more than 6 days of simulation time. The value reported in Tab. 3 is almost twice this estimation because the cell size is 1.5 µm for the REV simulation when it is 2 µm for the ST simulations, hence doubling the number of cells for the REV domains. If one would have used the non-stationary M$^{\mathrm{FE}}$ methodology instead, with typically 10 000 min · mm^{-1} (Tab. 2) and with cell size 1.5 µm, the anticipated simulation time for case #1 reaches more than 7 years, which would obviously be unrealistic, hence the effort to propose the hybrid methodologies.

Fig. 7 shows the computed grain structure in vertical cross-sections through the virtual REV. Similar maps as for Fig. 5 are drawn, making use of the normal vector to the cut to index the IPF color code, i.e. the **X** direction for the **YZ** cut in (a) and the **Y** direction for **XZ** cuts in (b-d). For Z coordinates lower than −65 µm, the grain structure of the substrate is maintained. It was not melted by the laser and conserves its grain density, n_s, and random crystallographic orientation. A transition progressively takes place above $Z = -65$ µm and up to approximately $Z = 200$ µm. This is clearly seen in Fig. 7 (a) and (c) by the progressive change of the color distribution in this zone, identifying a texture evolution

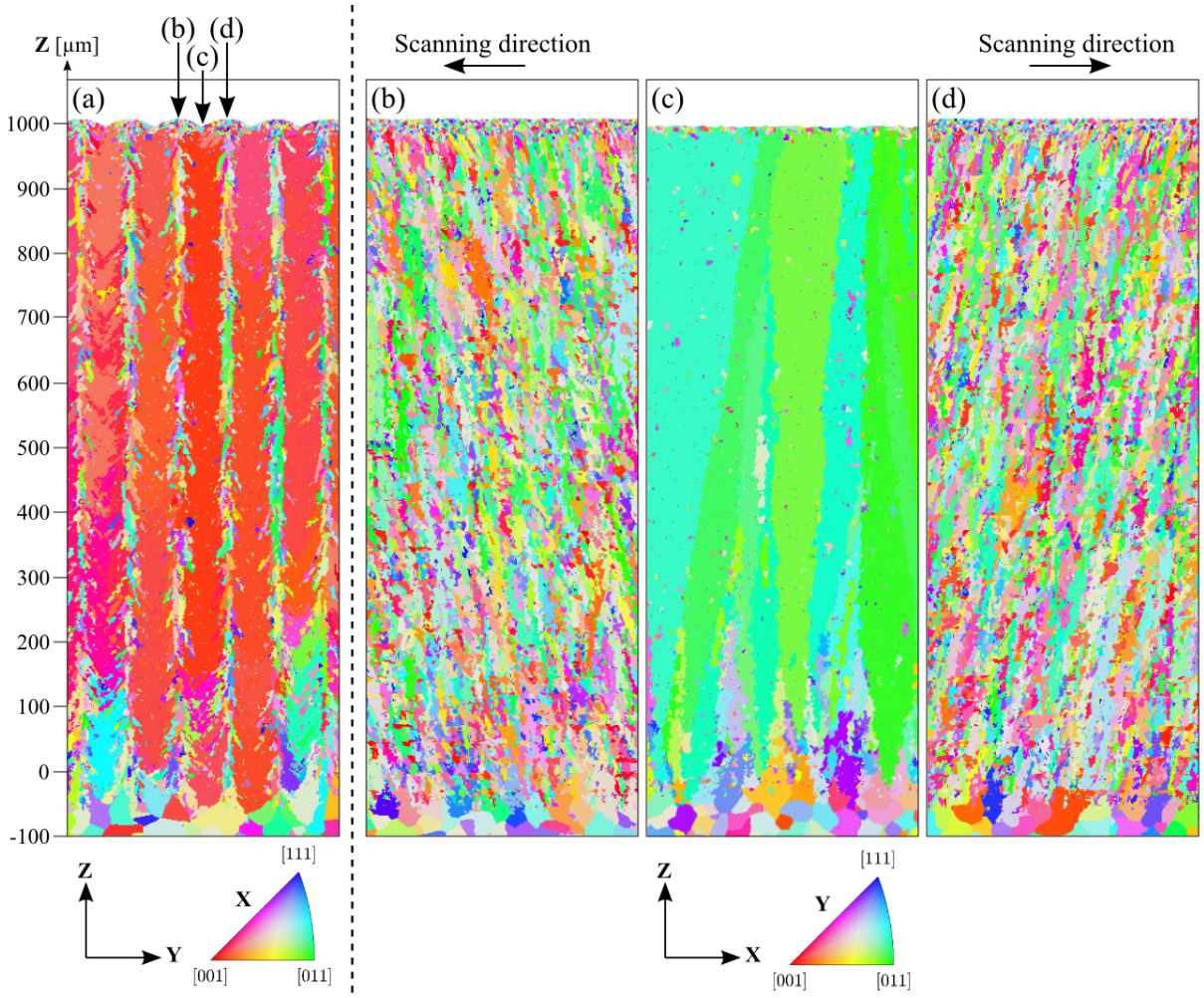

Figure 7: Computed grain structure in the case #1 REV built by L-PBF for an AMed component in IN718, referred to as the reference case (Tab. 3). IPF maps of (a-c) longitudinal cross-sections localized (b) between two tracks ($Y = 0.000\,\mu m$) and (a and c) half-hatch spacing apart from (b), i.e. at the center of the two tracks adjacent to (b), as shown in (d) the central transverse cross section ($X = 0.000\,\mu m$). Cross-sections are 420 µm wide, i.e. only the central part of the 600x600 μm^2 simulation domains are kept to avoid edge effects on the grain structure (Fig. 6), covering a height from $Z = -100\,\mu m$ and up to the top of the built part more than 1 mm above. Initial substrate at height $Z = 0\,mm$.

above the substrate. Above 200 µm, the grain structure is made of elongated grains which propagate across several layers. The map in Fig. 7(a) is perpendicular to the scanning direction. At the top of the REV, the consolidated tracks of the last layer clearly appear, with the peak of each arch coinciding with the constant Y trajectory of the laser and the valleys being found at mid-way between two scans, i.e. $Y \pm h_s/2$. The color in between two scans is found reddish. This indicates that the grains have a $\langle 100 \rangle$ crystallographic direction aligned with the **X** axis. If one considers the corresponding cut in Fig. 7(c) (see the position of the (c) cut indicated in the upper part of (a)), large zones with greenish and light blue colors are found above 200 µm, indicating $\langle 110 \rangle$ crystal directions aligned with the **Y** direction. Hence, the often reported texture in the literature is retrieved for the S_L^X scanning strategy, with large columns of elongated grains of width close to the hatch spacing [9, 16, 18, 17]. As a consequence of a $\langle 100 \rangle$ texture in the scanning **X** direction and a $\langle 110 \rangle$ texture in the **Y** direction, it is thus also expected a $\langle 110 \rangle$ texture in the building **Z** direction for the large grains between tracks. This is indeed found when considering the 3D reconstruction of a small cubic part of the computed REV displayed in Fig. 8(#1), where the top **Z** cut also reveals large greenish and light blue regions in between passes. This phenomenon has been highlighted several times for IN718 by experimental studies [9, 16, 17], and is also observed for other materials such as stainless steel 316L [84, 85].

In Fig. 7(a), above $Z = 200\,\mu m$, smaller grains can be observed between the large reddish zones. They form thin vertical bands aligned with the trajectories of the laser, i.e. with the peak of the arches. These grains are elongated along the building **Z** direction in Fig. 7(a) but are also tilted by approximately 10° toward the scanning direction in Fig. 7(b) and (d). Moreover, in the **Z** cut shown at the top surface of Fig. 8(#1), they appear as lines of small grains with a dominant reddish color, revealing a ⟨100⟩ crystal orientation mostly aligned with the **Z** axis. The color of these grains in Fig. 7 does not reveal additional preferred orientations.

To explain the origin of the grains, it is worth considering the structure under construction, as illustrated in the left of Fig. 9(#1). The melt pool shape of each individual track is highlighted by black dotted contours. The bottom part of these contours is the deepest position of isotherm T_L. Hence, as explained in Sect. 2.1, the normal to the bottom of the contours gives the direction of the temperature gradient. It is vertical, along the **Z** direction, at the very bottom of the pool, but it is misoriented by around 45° in the $+\mathbf{Y}$ (resp. $-\mathbf{Y}$) direction at the bottom left (resp. right) part of the melt pool. As a result of directional dendritic growth in cubic metals, the grains with ⟨100⟩ directions best aligned with the temperature gradient survive the growth competition. Consequently, at the lowest position of the melt pool, more reddish grains are observed in the **Z** IPF color coded Fig. 9(#1, left), forming the small reddish bands in **Z** cuts (Figs 8(#1) and 9(#1, center)). With the same color coded grain map, the large greenish and light blue bands in Fig. 9(#1) correspond to grains growing with a ⟨100⟩ direction at ±45° with respect to the **Z** direction, resulting from grain selection by the temperature gradient. Finally, it is worth mentioning that the top part of the track is made of a very fine population of grains that originate from nucleation in the undercooled melt at the rear of the liquid pool with a low G_L/v_L ratio. Most of these grains will yet be remelted as the laser builds the next layer. However, those of the grains that are located at the central bottom part of the melt pool are not remelted and are exposed to a mainly vertical and high temperature gradient (i.e. along the $+\mathbf{Z}$ direction), but also slightly tilted toward the scanning direction (see melt pool profile in Fig. 3), explaining the selection of grains with a ⟨100⟩ crystal direction aligned with the $+\mathbf{Z}$ direction and the slight tilt of approximately 10° toward the scanning direction of these selected grains in Fig. 7(b) and (d).

The ⟨100⟩ pole figure of the Z cut in the right hand part of Fig. 9(#1) is a simple but self-consistent representation of the above description. It provides information on the magnitude of the high textured construction resulting from the parameters of case REV #1. The same pole figures are found in the experimental study of the literature, which describes the same microstructure genesis mechanisms [17].

4.2. Overlapping ratio

In the present section, REV simulations with the S_L^X scanning strategy are considered. The goal is to discuss the effect of the overlapping ratio on the generated grain structure, estimated as the remelted width of adjacent tracks over the melt pool width, $r_0 = 1 - (h_s/w_m)$, the latter being the minimum width required to fully remelt the underneath surface. For that purpose, cases REV #1 to #4 are exploited. With case REV #1 as reference, a smaller hatch spacing characterizes REV #2, the laser power is decreased for REV #3 and the hybrid $\mathrm{H}^{\mathrm{Ros}}$ methodology is used for REV #4. As cases #1-#2 inherit from ST #A and #3 and #4 inherit from ST #D and #C, respectively, the w_m values are made accessible in Tab. 2 and the hatch distance in Tab. 3. One reaches the following r_0 values: (#1) 28 %, (#2) 53 %, (#3) 19 % and (#4) 50 %. These ratio are also easily visualized by the hidden width of the dotted contours in Fig. 9 over the half-hatch spacing listed in Tab. 3 (also the band width formed by the microstructure or the distance between the arch peaks at the top surface of the last layer).

In Fig. 9, a first observation for all cases is the presence of a persistent band of small grains below the laser scans with a common ⟨100⟩ crystallographic orientation aligned with the Z axis. The origin of these grains has already been explained in Sect. 4.1. It demonstrates the similar role of the strong vertical

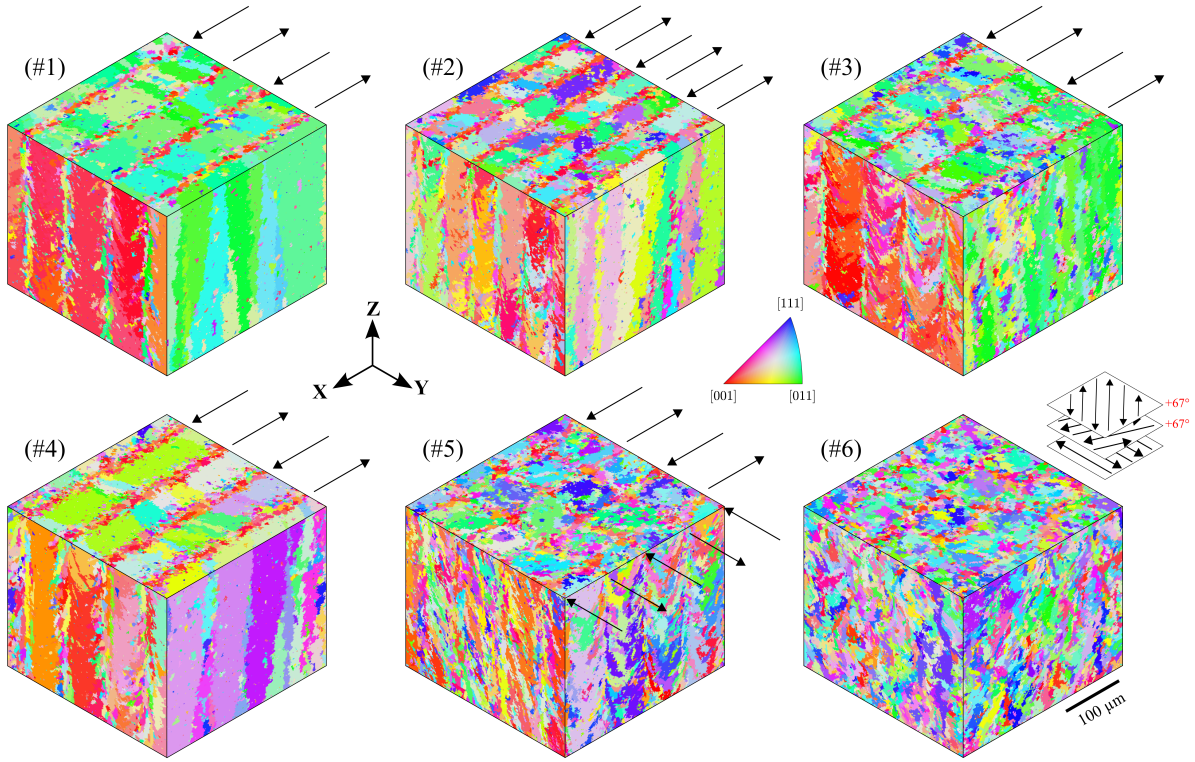

Figure 8: 3D cubic subdomains of size $300^3\,\mu m^3$ extracted at the center of the REV computed microstructure for IN718 built by L-PBF for cases #1 to #6 (Tab. 3). Arrows indicate the scan paths. On each face of the cubes, the IPF orientation is the corresponding normal.

temperature gradient at the bottom of the melt pool for all cases. Cases #1 and #3 have low values of the overlapping ratio. Their pole figures drawn in Fig. 9 also reveal close texture. Texture intensity is lower for case #3, thought, consequence of a more perturbed grain structure seen in Fig. 9(#3) and at the top surface of Fig. 8(#3), i.e. containing more blue grains. The same trend is retrieved in the transverse section of Fig. 8(#3) compared to (#1) (the **X** IPF color map), with less reddish colors and more perturbed distribution of orientations.

Cases REV #2 and #4 have similar values of the overlapping ratio, reaching around 50%. This is achieve either by decreasing the hatch spacing for case #2, with no change of the temperature field and the track width, or by considering the H^{Ros} methodology for case #4. Their corresponding pole density figures in Fig. 9 are also equivalent with several deviations from the reference case. First, a $\langle 100 \rangle$ direction is no longer pointing exactly in the $+\mathbf{Y} + \mathbf{Z}$ direction but instead approaches more the $+\mathbf{Y}$ direction. Second, the $\langle 100 \rangle$ directions of the grains that corresponds to the $-\mathbf{Y} + \mathbf{Z}$ direction in the reference case are now more distributed over several spots, close to each other, with a symmetry with respect to the **YZ** plane, and slightly closer to the $+\mathbf{Z}$ direction. As a consequence, the $\langle 100 \rangle$ texture in the $+\mathbf{X}$ direction is weaker, and not so well aligned with the scanning direction of the laser. This splitting of the texture may be linked to the alternate $+\mathbf{X}$ and $-\mathbf{X}$ scanning directions. Again, these differences in the texture of the REV are seen by the color distributions in Fig. 8 and Fig. 9.

Comparison is also possible by computing the grain density in successive **Z** cuts, i.e. at various heights, from the bottom of the substrate, at $Z = -100\,\mu m$, up to the top of the REV, at around $Z = 1000\,\mu m$. In practice, cuts are analyzed up to a lower position, $Z = 800\,\mu m$, in order to avoid reaching the non steady grain structure of last constructed layers. Similarly, the horizontal cross-sections analyzed have a size of $420^2\,\mu m^2$ centered with the whole section of the REV to avoid side effects in the analysis. Results are reported in Fig. 10. The grain density is found to remain constant for all simulation cases at a height

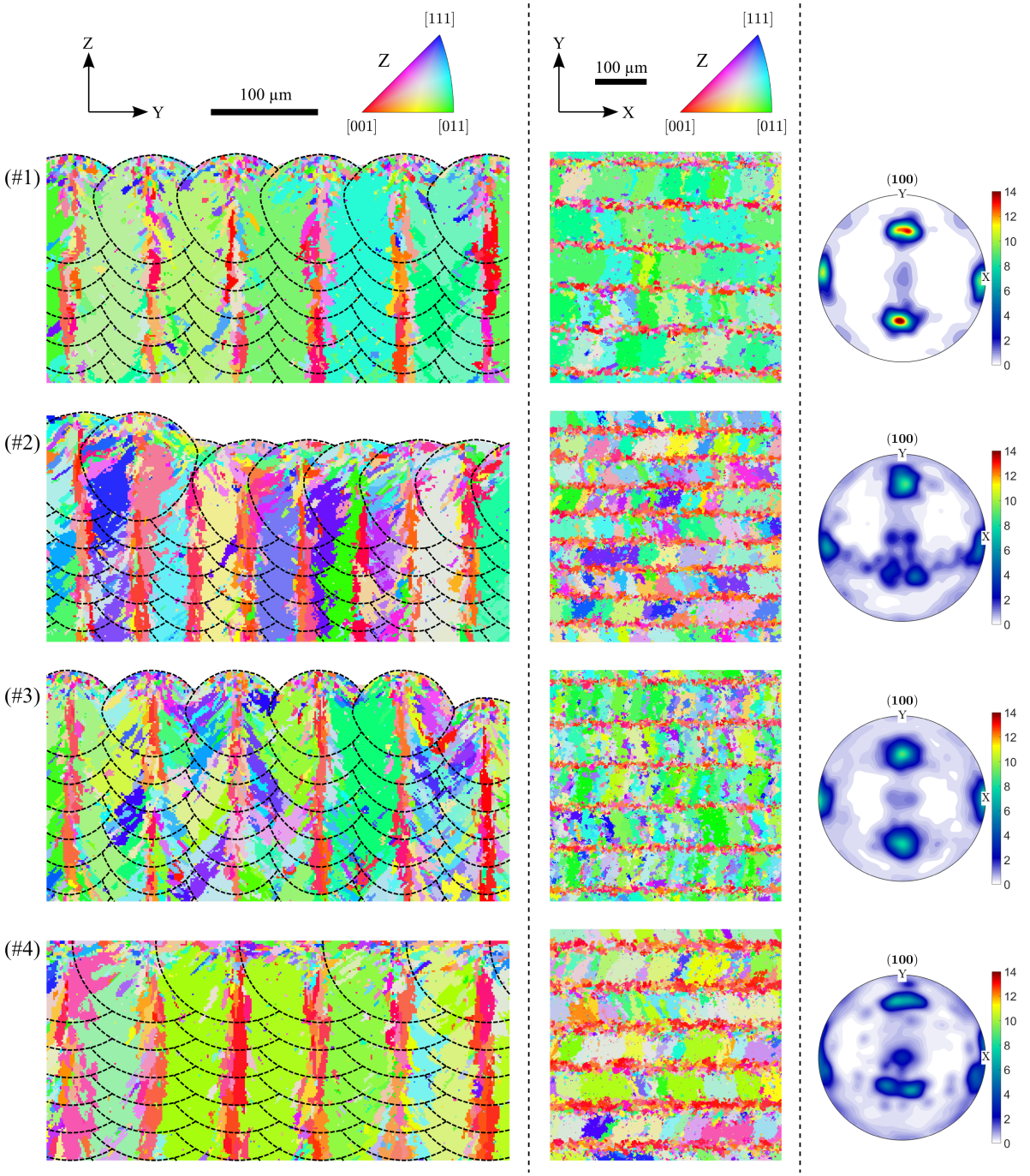

Figure 9: Small portion of the grain structure under construction colored with IPF maps using the **Z** axis showing (left) a transverse **X** cross-section taken at $\mathbf{X} = 300\,\mu\text{m}$ with the last solidified layers, (center) a horizontal **Z** cross-section taken 500 µm above the substrate and (right) the associated ⟨100⟩ pole density figure. The superimposed black dotted contours reveal the melt pool shape of each track. REV cases (#1) to (#4) are illustrated, as listed in Tab. 3. It is worth insisting on the choice of the **Z** direction for the IPF color map of the grain structure shown in the X cuts (at left).

higher than $Z \approx 500\,\mu\text{m}$. At steady state, REV #1 exhibits the lowest grain density and REV #3 the highest. For REV #3, the creation of new grains by nucleation is expected to be higher due to a smaller temperature gradient at the top rear of the undercooled melt (Fig. 3) when decreasing the power of the laser. The number of grains remelted during successive passes is also reduced due to a lower melt pool depth and a lower value of the overlapping ratio. At constant laser power, a greater overlapping ratio leads to a greater grain density. For cases #2 and #4, at each scan, almost half of the previous track is remelted. The small grains, located in the center of the previous track, are partially remelted and are

seeds for epitaxial growth in the ongoing track. For case #1, the small overlapping ratio makes each scan remelt larger grains so fewer grains can grow by epitaxy and the final density is found lower.

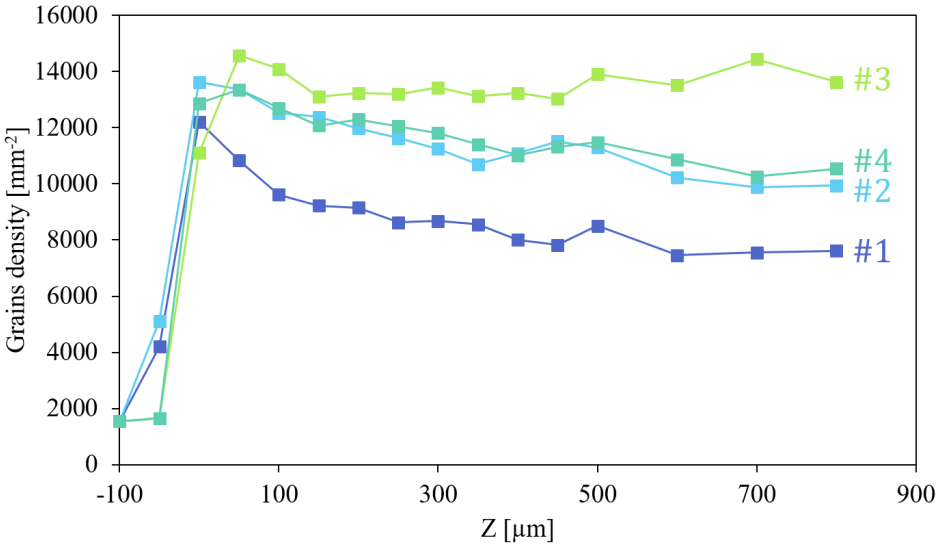

Figure 10: Grains density of REV simulations versus height in the REV #1 to #4 monodirectional scanning strategies S_L^X (Tab. 3).

4.3. Scanning strategy

The scanning strategy is analyzed considering the constant laser power of the reference case REV #1 and the same nucleation parameters. At first, the hatch spacing is considered. This result has already been introduced in section 4.2. A decrease of the hatch spacing reveals a strong change of the texture as well as an increase of the total grain density.

The second analysis is made by maintaining the hatch spacing but changing the scanning directions of the laser, i.e. using the S_L^{XY} strategy. This is accessible through the simulation of the REV #5 presented in Figs 8 and 11. All IPF maps are drawn while using the normal vector to the cross-sections as reference for the color code. Additionally, the pole density figure of the ⟨100⟩ crystallographic directions found in the horizontal **Z** cross-section drawn at 500 µm above the substrate is added to Fig. 11 for comparison with results in Fig. 9. A first observation is that the scanning strategy leaves its signature on the grain structure. As can be observed in the horizontal **Z** cross-section, small reddish grains with ⟨100⟩ crystallographic orientation aligned with the **Z** axis form bands along the **X** and **Y** scanning axes. This fine square grid and its associated texture is again very comparable with experimental data reported in the literature [16, 18, 86]. Between these lines, large grains of width close to h_s can be observed. However, these grains are less elongated than the one generated in case REV #1 and the **X** cross-sections does not show a strong fiber texture along the scanning directions of the laser (see also Fig. 8). The large grains have ⟨100⟩ crystallographic orientations forming a large angle with the Z direction, but not the simple components of the ±**YZ** or ±**XZ** directions as could have been expected from the study of the S_L^X strategy reported in Fig. 9(#1). This is coherent with the fact that, as the direction of the temperature gradient changes between two successive layers, the grain directions are more scattered compared with the reference case. As a result, reported final grain density is higher with the S_L^{XY} scanning strategy compared with the S_L^X scanning strategy, as shown in Fig. 12 by comparing the curves for cases REV#1 and #5.

Finally, the S_L^{67} scanning strategy is considered in Fig. 8(#6), Fig. 11 (#6) and Fig. 12 curve #6. The print of the scanning strategy on the arrangement of the grains is still visible but is less intense

and the final grain density is equivalent compared to the bidirectional strategy represented by REV #5, as shown in Fig. 12. With S_L^{XY} strategy, some grains can cross multiple layers, such as the one seen on the vertical cross sections (normal **X** or **Y**) of Fig. 8(#5) and 11(#5). This phenomenon is not found with the S_L^{67} strategy for which grains do not cross more than two layers. In case S_L^{XY}, the solidification conditions (distribution of the temperature gradient) are repeated one layer over two. If a grain is favorably oriented to grow vertically during the solidification of two consecutive layers, it will spread along the building direction. In case S_L^{67}, there is no repetitive solidification conditions. So at each layer, a new grain is selected to grow and stops the propagation of underlying grains. Even if a grain propagates through two layers, it will be stopped at the third one. This phenomenon makes REV #6 have a more isotropic structure than REV #5. These observations explains why the literature presents the S_L^{67} scanning strategy as a way to almost cancel texture formation in AMed components.

4.4. Grain density

Simulation cases for REV #7 to #12 were finally run to analyze the influence of the nucleation density in the undercooled melt and the grain density of the substrate for both scanning strategy S_L^X and S_L^{XY}. In simulation cases REV #7 and #8, the nucleation density in the melt, $n_V = 1 \times 10^6\,\mathrm{mm}^{-3}$, is decreased by one order of magnitude compared to the reference case REV #1. It is further decreased to $n_V = 0\,\mathrm{mm}^{-3}$ for cases REV #9 and #10. Thus, while maintaining the S_L^X strategy, the nucleation density decreases from case #1 to case #7 and then to case #9, leading to a progressive lower final grain density revealed in the curves of Fig. 12. The same behavior is found while maintaining the S_L^{XY} strategy with cases #5, #8 and #10. In all cases, the influence of the scanning strategy for a given nucleation density in the melt also retrieves the observation for curves #1 and #5, i.e. curves #7 and #8 for $n_V = 1 \times 10^6\,\mathrm{mm}^{-3}$ and curves #9 and #10 for $n_V = 0\,\mathrm{mm}^{-3}$ show higher grain density for S_L^{XY} compared to S_L^X. This evolution is expected as the change from S_L^X to S_L^{XY} limits epitaxial grain growth and provide better efficiency of the nucleation process. Figs 11(#9) and (#10) show the IPF maps of transverse and horizontal cross-sections with suspended nucleation events in the undercooled melt. In other words, all grains seen in these figures where initially present in the substrate and could freely develop in the whole REVs. Despite the absence of nucleation events, the same trends is found for case REV #9, with selection of the grains initially present in the substrate that organize to approach the texture of case REV #1. However, because of the very low grain density, the texture is more diffuse as is shown by the corresponding pole density figures. Also the thin bands of grains have almost vanished, which is not surprising as they outcome from nucleation and selection of the newly formed grains in the melt in REV #1. Finally, comparison of cases REV #5 and #10 in Fig. 11 shows similar trends as the one presented for cases REV #1 and #9. The squared arrangement of the grains is still clearly visible but is more subject to randomness as it adapts to the initial low grain density of the substrate.

The final study concerns the initial substrate density, n_S. In simulation case #11, a single crystal is used but the nucleation density in the melt is maintained at its reference value. Fig. 13 reveals that, very rapidly, the same evolution of the grain density is reached, hence cancelling the role of the substrate and revealing the predominant role of the nucleation in the melt. On the contrary, simulation case REV #12 is run with a very high grain density of the substrate but suspending nucleation in the undercooled liquid. Fig. 13 shows that the grain density drops very rapidly with height to reach the grain density of the simulation case #9 at $Z \approx 300\,\mu\mathrm{m}$. Again, it can be concluded that the role of the substrate grain density is minor compared to that of the nucleation density in the melt.

5. Conclusions

A new hybrid methodology for the CA model is presented and applied to predict grain structures in AMed REV of IN718 generated by L-PBF. The modeling of large REV is made possible thanks to the

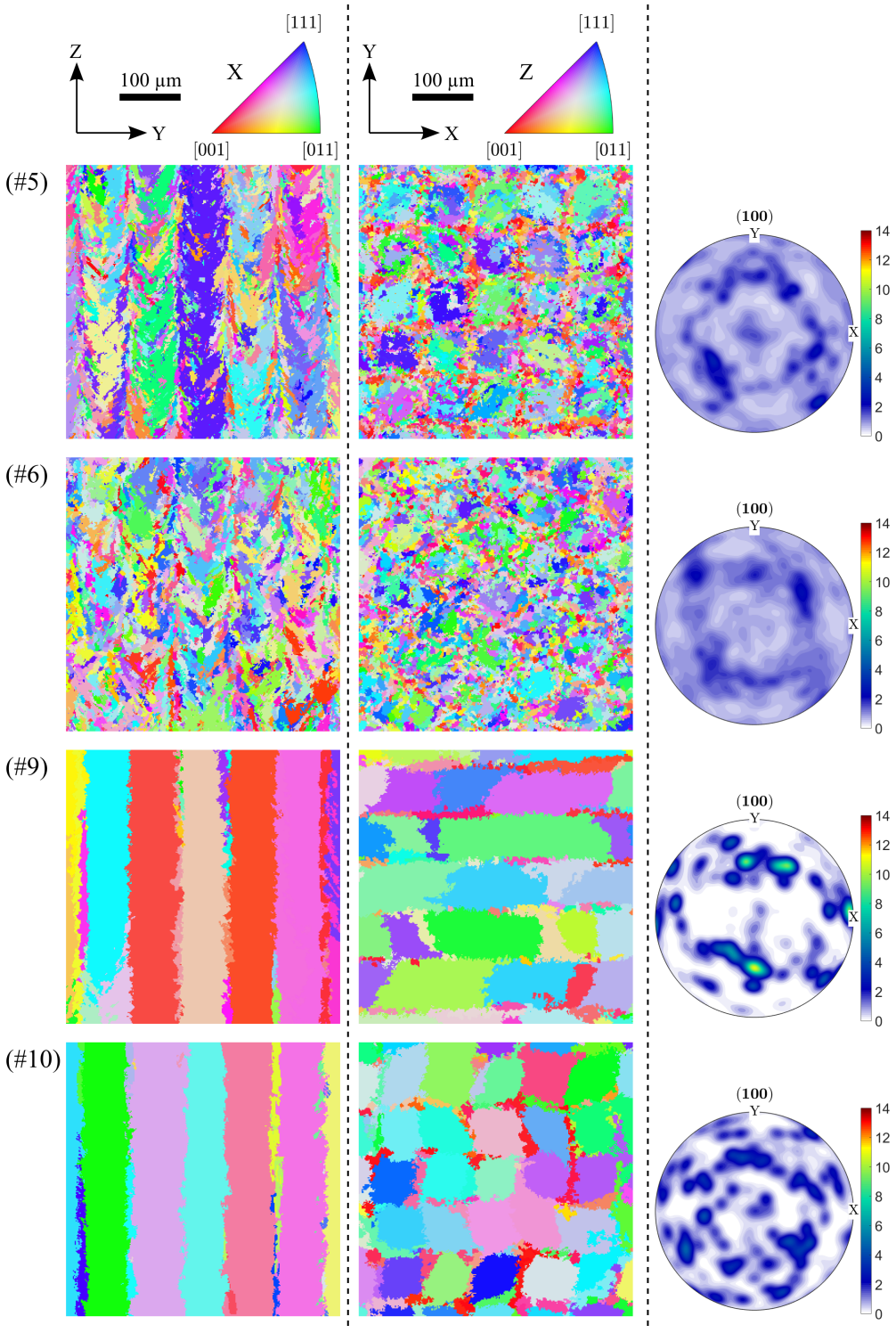

Figure 11: Grain structure with IPF color code using the normal vector to the cut, with (left) transverse cross-sections (normal to **X**), (center) horizontal cross-sections (normal **Z**) at height 500 µm above the substrate and (right) associated pole density figures. Cases are for REV #5, #6, #9 and #10. (Tab. 3)

use of a steady state consolidated track shape and temperature field deduced from a predetermined full thermohydraulic numerical solution applied to a single linear track. The solution includes the role of the various forces acting on the liquid pool (e.g. recoil pressure, Marangoni convection, surface tension) but also processing parameters (e.g., power, velocity and radius of the laser, thickness of the powder bed). The thermohydraulic numerical solution based on the FE method was already validated [71,

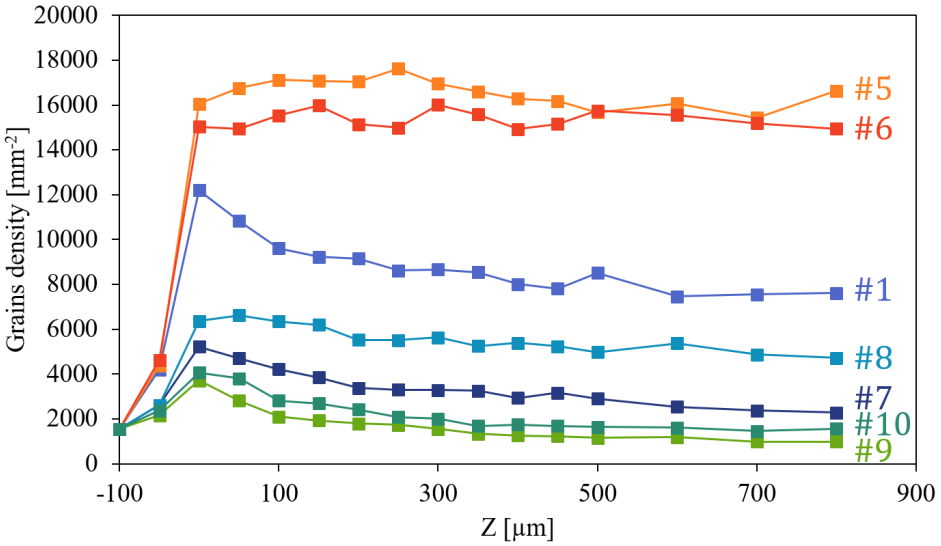

Figure 12: Grains density of REV simulations versus height in the multidirectional scanning strategies (#5, #7-#10) S_L^{XY} and (#6) S_L^{67} compared to the monodirectional scanning strategy S_L^X (#1) (Tab. 3).

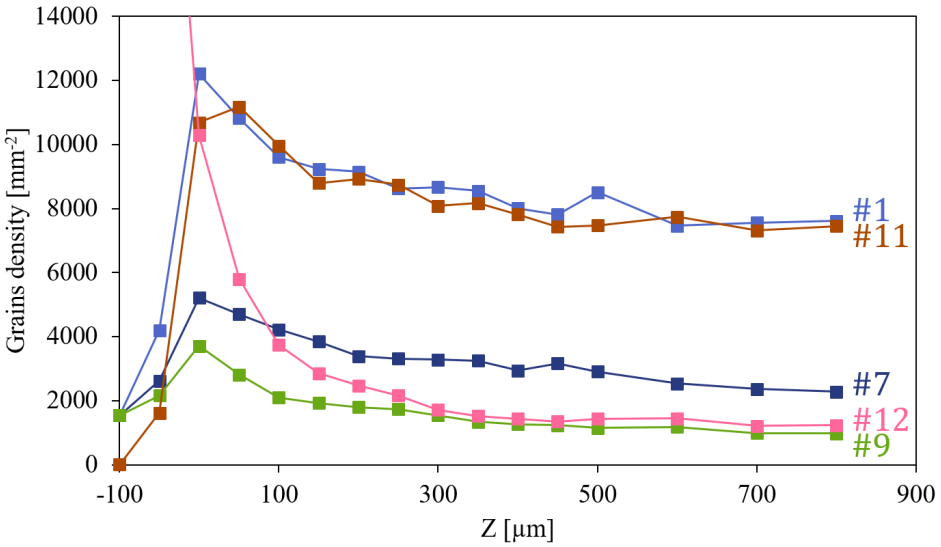

Figure 13: Grains density of REV simulations versus height in the REV #1, #7, #9, #11-#12 (Tab. 3).

72, 73, 74]. Results are then stored and exploited in a versatile manner to compute grain structures resulting from multitrack multilayer scanning strategies. The parameters of the CA model becomes the hatch spacing as well as the directions of the laser trajectory within each layer, but also its change from one layer to the other. Comparison of grain structure with measurements in the literature show good agreement concerning crystallographic textures and grain density evolution as a function of the processing parameters. Comparisons of the model using numerical and analytical solutions is also carried out. Because the grain structure is greatly influenced by the temperature field, recommendation is to prefer simulation deduced from the numerical solution. The study also demonstrates that the grain structure far enough from the substrate does not depend on the substrate as it mainly results from the competition between nucleation and growth of the grains that were created in the undercooled melt. Finally, the effect of changing the scanning directions from one layer to the other retrieves the reduction of the crystallographic texture and an increase of the grain density reported in the literature. Simulation also includes a case with a 67° rotation of the scanning directions around the building direction at each

new layer, a common industrial practice for which simulation was not reported in the literature so far.

The new hybrid methodology presented in this article makes accessible more than 200 mm long scans to built a 3D REV. Up to now, the geometry are only cubic domains, with typically less than 1 mm^3. However, the model is based on the FE method using unstructured mesh so there is no restriction to assess grain structure simulations in a complex geometry, e.g. an IN718 impeller made of several blades [61]. The only limitation becomes the volume of the simulation domain that one could assess. At present, the dimensions of such a complex geometry should be limited to only few cubic millimeters. Beside studying the generated grain structure, an other reasonable exploitation of the model is through its coupling with prediction of the material properties, including its mechanical response to solicitation considering its texture [6, 7, 4, 11, 14]. Propagation of ultrasound waves in the polycrystalline REV would also be of interest as it becomes a standard methodology to characterize AMed components [87, 88]. These directions are presently under investigations.

6. Acknowledgements

This research is supported by the Centre Technique des Industries Mécaniques (Cetim, 7 rue de la Presse, 42000 Saint-Etienne, France) and the platform Additive Factory Hub (AFH, CEA Saclay Digiteo Labs, 91191 Gif-sur-Yvette, France).

References

[1] I. Gibson, D. Rosen, and B. Stucker. *Additive manufacturing technologies: 3D Printing, Rapid Prototyping and Direct Digital Manufacturing, 2nd Edition*. Springer New York Heidelberg Dordrecht London, 2015.

[2] P. Peyre and E. Charkaluk. *La fabrication additive des alliages métalliques*. iSTE editions London, 2022.

[3] C. Y. Yap, C. K. Chua, Z. L. Dong, Z. H. Liu, D. Q. Zhang, L. E. Loh, and S. L. Sing. Review of selective laser melting: Materials and applications. *Applied Physics Reviews*, 2(4):041101, 2015.

[4] Y. Lu, S. Wu, Y. Gan, T. Huang, C. Yang, L. Junjie, and J. Lin. Study on the microstructure, mechanical property and residual stress of SLM Inconel-718 alloy manufactured by differing island scanning strategy. *Optics & Laser Technology*, 75:197–206, 2015.

[5] K.A. Mumtaz, P. Erasenthiran, and N. Hopkinson. High density selective laser melting of waspaloy. *Journal of Materials Processing Technology*, 195:77–87, 2008.

[6] K.N. Amato, S.M. Gaytan, L.E. Murr, E. Martinez, P. W. Shindo, J. Hernandez, and F. Collins, S. ad Medina. Microstructures and mechanical behavior of inconel 718 fabricated by selective laser melting. *Acta Materialia*, 60:2229–2239, 2012.

[7] Z. Wang, K. Guan, M. Gao, X. Li, X. Chen, and X. Zeng. The microstructure and mechanical properties of deposited-in718 by selective laser melting. *Journal of Alloys and Compounds*, 513:518–523, 2012.

[8] B. Vayre. *Conception pour la fabrication additive, application à la technologie EBM*. Thèse de doctorat, Université de Grenoble, 2014.

[9] J.-P. Choi, G.-H. Shin, S. Yang, D.-Y. Yang, J.-S. Lee, M. Brochu, and J.-H. Yu. Densification and microstructural investigation of Inconel 718 parts fabricated by selective laser melting. *Powder Technology*, 310:60–66, 2017.

[10] M. Sadowski, L. Ladani, W. Brindley, and J. Romano. Optimizing quality of additively manufactured inconel 718 using powder bed laser melting process. *Additive Manufacturing*, 11:60–70, 2016.

[11] T. Trosch, J. Ströβner, R. Völkl, and U. Glatzel. Microstructure and mechanical properties of selective laser melted inconel 718 compared to forging and casting. *Materials Letters*, 164:428–431, 2016.

[12] X. Wang, T. Keya, and K. Chou. Build height effect on the inconel 718 parts fabricated by selective laser melting. *Procedia Manufacturing*, 5:1006–1017, 2016.

[13] Q.B. Nguyen, M.L.S. Nai, Z. Zhu, C.-N. Sun, J. Wei, and W. Zhou. Characteristics of inconel powders for powder-bed additive manufacturing. *Engineering*, 3:695–700, 2017.

[14] S. Holland, X. Wang, J. Chen, W. Cai, F. Yan, and L. Li. Multiscale characterization of microstructures and mechanical properties of Inconel 718 fabricated by selective laser melting. *Journal of Alloys and Compounds*, 784:182–194, 2019.

[15] D. S. Watring, J. T. Benzing, N. Hrabe, and A. D. Spear. Effects of laser-energy density and build orientation on the structure–property relationships in as-built Inconel 718 manufactured by laser powder bed fusion. *Additive Manufacturing*, 36:101425, 2020.

[16] N. Nadammal, T. Mishurova, T. Fritsch, I. Serrano-Munoz, A. Kromm, C. Haberland, P.D. Portella, and G. Bruno. Critical role of scan strategies on the development of microstructure, texture, and residual stresses during laser powder bed fusion additive manufacturing. *Additive Manufacturing*, 38:101792, 2021.

[17] O. Gokcekaya, T. Ishimoto, S. Hibino, J. Yasutomi, T. Narushima, and T. Nakano. Unique crystallographic texture formation in Inconel 718 by laser powder bed fusion and its effect on mechanical anisotropy. *Acta Materialia*, 212:116876, 2021.

[18] L. Lacoste, A. Sakly, S. Dépinoy, S. Lebel, B. Vayre, and C. Colin. Microstructure control of additively manufactured in718 by l-pbf process. *Powder Metallurgy*, 2022, in press.

[19] D. Rosenthal. The theory of moving sources of heat and its application to metal treatments. *Transactions of the ASME*, 68:849, 1946.

[20] H.E. Cline and T.R. Anthony. Heat treating and melting material with a scanning laser or electron beam. *Journal of Applied Physics*, 48:3895–3900, 1977.

[21] P. Promoppatum, S.-C. Yao, P.C. Pistorius, and A.D. Rollett. A comprehensive comparison of the analytical and numerical prediction of the thermal history and solidification microstructure of inconel 718 products made by laser powder-bed fusion. *Engineering*, 3:685–694, 2017.

[22] J. A. Koepf, M. R. Gotterbarm, M. Markl, and C. Körner. 3D multi-layer grain structure simulation of powder bed fusion additive manufacturing. *Acta Materialia*, 152:119–126, 2018.

[23] J.A. Dantzig and M. Rappaz. *Solidification, 2nd Edition.* EPFL Press, Lausanne, Switzerland, 2016.

[24] W. Kurz and D.J. Fisher. *Fundamentals of Solidification, 3rd edition.* Trans Tech Publications, Aedermannsdorf, Switzerland, 1989.

[25] J.D. Hunt. Steady state columnar and equiaxed growth of dendrites and eutectics. *Materials Science and Engineering*, 65:75–83, 1984.

[26] M. Gaümann, C. Bezençon, P. Canalis, and W. Kurz. Single-crystal laser deposition of superalloys: processing-microstructure maps. *Acta Materialia*, 49:1051–1062, 2001.

[27] Y. He, M. Zhong, N. Jones, J. Beuth, and B. Webler. The Columnar-to-Equiaxed Transition in Melt Pools During Laser Powder Bed Fusion of M2 Steel. *Metallurgical and Materials Transactions A*, 52(9):4206–4221, 2021.

[28] P. Mohammadpour and A. B. Phillion. Solidification microstructure selection maps for laser powder bed fusion of multicomponent alloys. *IOP Conference Series: Materials Science and Engineering*, 861(1):012005, 2020.

[29] J. P. Oliveira, A. D. LaLonde, and J. Ma. Processing parameters in laser powder bed fusion metal additive manufacturing. *Materials & Design*, 193:108762, 2020.

[30] J.H.K. Tan, S.L. Sing, and W.Y. Yeong. Microstructure modelling for metallic additive manufacturing: a review. *Virtual and Physical Prototyping*, pages 1–19, 2019.

[31] C. Körner, M. Markl, and J.A. Koepf. Modeling and simulation of microstructure evolution for additive manufacturing of metals: a critical review. *Metallurgical and Materials Transactions*, 51A:4970–4983, 2020.

[32] R. Echebarria, R. Folch, A. Karma, and M. Plapp. Quantitative phase-field model of alloy solidification. *Phys. Rev. E*, 70:22, 2004.

[33] T. Takaki, S. Sakane, M. Ohno, Y. Shibuta, T. Aoki, and C.-A. Gandin. Competitive grain growth during directional solidification of a polycrystalline binary alloy: Three-dimensional large-scale phase-field study. *Materialia*, 1:104–113, 2018.

[34] T. Keller, G. Lindwall, S. Ghosh, L. Ma, B. M. Lane, F. Zhang, U. R. Kattner, E. A. Lass, J. C. Heigel, Y. Idell, M. E. Williams, A. J. Allen, J. E. Guyer, and L. E. Levine. Application of finite element, phase-field, and CALPHAD-based methods to additive manufacturing of Ni-based superalloys. *Acta Materialia*, 139:244–253, 2017.

[35] X. Wang and K. Chou. Microstructure simulations of Inconel 718 during selective laser melting using a phase field model. *The International Journal of Advanced Manufacturing Technology*, 100(9):2147–2162, 2019.

[36] A. F. Chadwick and P. W. Voorhees. The development of grain structure during additive manufacturing. *Acta Materialia*, 211:116862, 2021.

[37] I. Steinbach, C. Beckermann, B. Kauerauf, Q. Li, and J. Guo. Three-dimensional modeling of equiaxed dendritic growth on a mesoscopic scale. *Acta Materialia*, 47:971–982, 1999.

[38] I. Steinbach, H.-J. Diepers, and C. Beckermann. Transient growth and interaction of equiaxed dendrites. *Acta Materialia*, 275:624–638, 2005.

[39] Y. Souhar, V.F. De Felice, C. Beckermann, H. Combeau, and M. Zaloznik. Three-dimensional mesoscopic modeling of equiaxed dendritic solidification of a binary alloy. *Computational Materials Science*, 112:304–317, 2016.

[40] A. Olmeda, M. Zaloznik, and H. Combeau. Quantitative 3d mesoscopic modeling of grain interactions during equiaxed dendritic solidification in a thin sample. *Acta Materialia*, 173:249–261, 2019.

[41] D. Tourret and A. Karma. Multiscale dendritic needle network model of alloy solidification. *Acta Materialia*, 61:6474–6491, 2013.

[42] D. Tourret and A. Karma. Three-dimensional dendritic needle network model for alloy solidification. *Acta Materialia*, 120:240–254, 2016.

[43] D. Tourret, M.M. Francois, and A.J. Clarke. Multiscale dendritic needle network model of alloy solidification with

fluid flow. *Computational Materials Science*, 162:206–227, 2019.

[44] R. Fleurisson, O. Senninger, G. Guillemot, and Ch.-A. Gandin. Hybrid cellular automaton - parabolic thick needle model for equiaxed dendritic solidification. *Journal of Materials Science & Technology*, 124:26–40, 2022.

[45] T. M. Rodgers, J. D. Madison, V. Tikare, and M.C. Maguire. Predicting mesoscale microstructural evolution in electron beam welding. *JOM*, 68:1419–1426, 2016.

[46] T. M. Rodgers, J. D. Madison, and V. Tikare. Simulation of metal additive manufacturing microstructures using kinetic Monte Carlo. *Computational Materials Science*, 135:78–89, 2017.

[47] T. M. Rodgers, D. Moser, F. Abdeljawad, O.D. Underwood Jackson, J.D. Carroll, B.H. Jared, D.S. Bolintineanu, J.A. Mitchell, and J. D. Madison. Simulation of powder metal additive manufacturing microstructures with coupled finite difference-monte carlo method. *Additive Manufacturing*, 41:101953, 2021.

[48] S. Sunny, H. Yu, R. Mathews, A. Malik, and W. Li. Improved grain structure prediction in metal additive manufacturing using a dynamic kinetic monte carlo framework. *Additive Manufacturing*, 37:101649, 2021.

[49] W. Kurz, B. Giovanolla, and R. Trivedi. Theory of microstructural development during rapid solidification. *Acta Metallurgica*, 34:823–830, 1986.

[50] O. Hunziker. Theory of plane front and dendritic growth in multicomponent alloys. *Acta Materialia*, 49(20):4191–4203, 2001.

[51] G. Guillemot, O. Senninger, C. A. Hareland, P. W. Voorhees, and Ch.-A. Gandin. Thermodynamic coupling in the computation of dendrite growth kinetics for multicomponent alloys. *Calphad: Computer Coupling of Phase Diagrams and Thermochemistry*, 77:102429, 2022.

[52] M. Rappaz and Ch.-A. Gandin. Probabilistic modelling of microstructure formation in solidification processes. *Acta Materialia*, 41:345–360, 1993.

[53] Ch.-A. Gandin and M. Rappaz. A coupled finite element-cellular automaton model for the prediction of dendritic grain structures in solidification processes. *Acta Materialia*, 42:2233–2246, 1994.

[54] Ch.-A. Gandin and M. Rappaz. A 3d cellular automaton algorithm for the prediction of dendritic grain growth. *Acta Materialia*, 45(5):2187–2195, 1997.

[55] A. Rai, M. Markl, and C. Körner. A coupled Cellular Automaton–Lattice Boltzmann model for grain structure simulation during additive manufacturing. *Computational Materials Science*, 124:37–48, 2016.

[56] A. Zinoviev, O. Zinovieva, V. Ploshikhin, V. Romanova, and R. Balokhonov. Evolution of grain structure during laser additive manufacturing. Simulation by a cellular automata method. *Materials & Design*, 106:321–329, 2016.

[57] O. Zinovieva, A. Zinoviev, and V Ploshikhin. Three-dimensional modeling of the microstructure evolution during metal additive amnufacturing. *Computatinoal Materials Science*, 141:207–220, 2018.

[58] J. Yang, H. Yu, H. Yang, F. Li, Z. Wang, and X. Zeng. Prediction of microstructure in selective laser melted ti-6al-4v alloy by cellular automaton. *Journal of Alloys and Compounds*, 748:281–290, 2018.

[59] J. A. Koepf, D. Soldner, M. Ramsperger, J. Mergheim, M. Markl, and C. Körner. Numerical microstructure prediction by a coupled finite element cellular automaton model for selective electron beam melting. *Computational Materials Science*, 162:148–155, 2019.

[60] Y. Lian, Z. Gan, C. Yu, D. Kats, W. K. Liu, and G. J. Wagner. A cellular automaton finite volume method for microstructure evolution during additive manufacturing. *Materials and Design*, 169:107672, 2019.

[61] Y. Zhang and J. Zhang. Modeling of solidification microstructure evolution in laser powder bed fusion fabricated 316l stainless steel using combined computational fluid dynamics and cellular automaton. *Additive Manufacturing*, 28:750–765, 2019.

[62] M.S. Mohebbi and V. Ploshikhin. Implementation of nucleation in cellular automaton simulation of microstructural evolution during additive manufacturing of al alloys. *Additive Manufacturing*, 36:101726, 2020.

[63] O. Zinovieva, A. Zinoviev, V. Romanova, and R. Balokhonov. Three-dimensional analysis of grain structure and texture of additively manufactured 316L austenitic stainless steel. *Additive Manufacturing*, 36:101521, 2020.

[64] K. Teferra and D. J. Rowenhorst. Optimizing the cellular automata finite element model for additive manufacturing to simulate large microstructures. *Acta Materialia*, 213:116930, 2021.

[65] S. Chen, G. Guillemot, and Ch.-A. Gandin. Three-dimensional cellular automaton-finite element modeling of solidification grain structures for arc-welding processes. *Acta Materialia*, 115:448–467, 2016.

[66] C. Xue, N. Blanc, F. Soulié, C. Bordreuil, F. Deschaux-Baume, G. Guillemot, M. Bellet, and Ch.-A. Gandin. Structure and texture simulations in fusion welding processes - comparison with experimental data. *Materialia*, 21:101305, 2022.

[67] S. Mosbah, M. Bellet, and Ch.-A. Gandin. Experimental and numerical modeling of segregation in metallic alloys. *Metallurgical and materials transactions*, 41:651–669, 2010.

[68] T. Carozzani, Ch.-A. Gandin, and H. Digonnet. Optimized parallel computing for cellular automaton-finite element modeling of solidification grain structures. *Modelling and Simulation in Materials Science and Engineering*, 22:015012, 2014.

[69] A. Pineau, G. Guillemot, D. Tourret, A. Karma, and Ch.-A. Gandin. Growth competition between columnar dendritic grains - cellular automaton versus phase field modeling. *Acta Materialia*, 155:286–301, 2018.

[70] E. Dorari, K. Ji, G. Guillemot, Ch.-A. Gandin, and A. Karma. Growth competition between columnar dendritic grains

- the role of microstructural length scales. *Acta Materialia*, 223:117395, 2022.

[71] Q. Chen, G. Guillemot, Ch.-A. Gandin, and M. Bellet. Three-dimensional finite element thermomechanical modeling of additive manufacturing by selective laser melting for ceramic materials. *Additive Manufacturing*, 16:124–137, 2017.

[72] L. Moniz, Q. Chen, G. Guillemot, M. Bellet, Ch.-A. Gandin, Ch. Colin, J.-D. Bartout, and M.-H. Berger. Additive manufacturing of an oxide ceramic by laser beam melting—comparison between finite element simulation and experimental results. *Journal of Materials Processing Tech.*, 270:106–117, 2019.

[73] A. Queva, G. Guillemot, C. Moriconi, and M. Metton, C.and Bellet. Numerical study of the impact of vaporisation on melt pool dynamics in Laser Powder Bed Fusion - Application to IN718 and Ti–6Al–4V. *Additive Manufacturing*, 35:101249, 2020.

[74] D. Grange, A. Queva, G. Guillemot, M. Bellet, J. D. Bartout, and C. Colin. Effect of processing parameters during the laser beam melting of Inconel 738: Comparison between simulated and experimental melt pool shape. *Journal of Materials Processing Technology*, 289:116897, 2021.

[75] A. A. Samokhin. Effect of laser radiation on absorbing condensed matter. *Proceedings of the Institute of General Physics Academy of Sciences of the USSR, Series Editor: AM Prokhorov*, 13:203, 1990.

[76] K. W. Kolasinski. *Surface science : foundations of catalysis and nanoscience*. John Wiley & Sons, 2012.

[77] J. U. Brackbill, D. B. Kothe, and Zemach C. A continuum method for modeling surface tension. *Journal of Computational Physics*, 100:335–354, 1992.

[78] J. G. Pauza, W. A. Tayon, and A. D. Rollett. Computer simulation of microstructure development in powder-bed additive manufacturing with crystallographic texture. *Modelling and Simulation in Materials Science and Engineering*, 29(5):055019, 2021.

[79] H.-J. Bunge. *Texture Analysis in Materials Science: Mathematical Methods*. Elsevier, 2013.

[80] J.-O. Andersson, T. Helander, L. Höglund, P. Shi, and B. Sundman. Thermo-calc & dictra, computational tools for materials science. *Calphad*, 26(2):273–312, 2002.

[81] Library PhysalurgY, KIND tool, https://physalurgy.cemef.mines-paristech.fr/.

[82] Thermocalc database TCNI10 \Ni-Alloys v10.0, Thermo-Calc Software AB, Sweden, 2021.

[83] Thermocalc database MOBNI5 \Ni-Alloys Mobility v5.1 , Thermo-Calc Software AB, Sweden, 2021.

[84] O. Andreau, I. Koutiri, P. Peyre, J.-D. Penot, N. Saintier, E. Pessard, T. De Terris, C. Dupuy, and T. Baudin. Texture control of 316L parts by modulation of the melt pool morphology in selective laser melting. *Journal of Materials Processing Technology*, 264:21–31, 2019.

[85] S. Dépinoy. Influence of solidification conditions on chemical heterogeneities and dislocations patterning in additively manufactured 316L stainless steel. *Materialia*, 24:101472, 2022.

[86] S.-H. Sun, K. Hagihara, and T. Nakano. Effect of scanning strategy on texture formation in Ni-25at.%Mo alloys fabricated by selective laser melting. *Materials & Design*, 140:307–316, 2018.

[87] J. Laurent, D. Royer, and C. Prada. In-plane backward and zero group velocity guided modes in rigid and soft strips. *Journal of the Acoustical Society of America, Acoustical Society of America*, 147:1302–1310, 2020.

[88] X. Bai, B. Tie, J.-H. Schmitt, and D. Aubry. Comparison of ultrasonic attenuation within two- and three-dimensional polycrystalline media. *Ultrasonics*, 100:105980, 2020.